Behavioral modeling of coordinated movements in brittle stars with a variable number of arms

（腕数に個体差があるクモヒトデの協調運動の行動モデリング）

A doctoral thesis

presented to the

Biosystems Science Course,
Division of Life Science,
Graduate School of Life Science,
Hokkaido University

by

Daiki Wakita

in

March 2020

CONTENTS

ACKNOWLEDGMENTS

My first appreciation goes to Prof. Hitoshi Aonuma (Hokkaido University) for supervising my doctoral research. I thank Prof. Masakane Yamashita and Prof. Makoto Mizunami for critically examining my doctoral thesis. I am grateful to Dr. Yumino Hayase (Hiroshima University) for motivating me to study mathematical modeling and pray that she may rest in peace. I thank Dr. Katsushi Kagaya (Kyoto University) for deeply and repeatedly discussing the theory of Bayesian statistics. I thank to Prof. Takeshi Kano (Tohoku University) for his fresh ideas on physics and robotics application of the behavior of brittle stars. I thank Dr. Takayuki Watanabe (Hokkaido University) for his critical and multi-aspect opinions to improve my study. I thank Mr. Keisuke Naniwa (Hokkaido University) for his great knowledge of programming and robotics. I thank Mr. Keita Harada (Shirahama Aquarium) for sending me the fresh individuals of brittle stars from the aquarium. I thank Prof. Philip L. Newland (University of Southampton) for his critical comment upon my manuscript for journal publication. Finally, my special appreciation goes to my family for always supporting my life.

1. GENERAL INTRODUCTION

This study shows how intraspecific morphological variation affects movement coordination in animals, focusing on the behavior of brittle stars, in which a drastic individual difference can be found in the number of radially symmetric body parts.

1.1 Body networks coordinating animal movements

Animals exhibit a variety of coordinated rhythmic movements, such as locomotion (e.g., crawling, walking, swimming, flying), mastication, ventilation, and heartbeat. Coordinated patterns in an animal body can change depending on the situation. For example, a horse increasing the moving speed firstly walks, then trots, then canters, and finally gallops (Alexander 1984). It is generally accepted that animals utilize neural activity, which is mediated by electrical signals (Hodgkin & Huxley 1952), to coordinate the movements of several body parts. Electrophysiological experiments have enabled us to illustrate synaptic interactions between several neurons that output coordinated movements, such as the chewing movements of gastric mill in lobsters (Mulloney & Selverston 1974a,b; Selverston & Mulloney 1974) and the heartbeat of leeches (Calabrese 1977; Hill et al. 2002). Computer simulations using mathematical models based on *in vitro* and *vivo* results have clearly explained complex neural networks, represented by those underlying the swimming patterns of lampreys (Grillner et al. 1991; Wadden et al. 1997; Ekeberg & Grillner 1999; Grillner 2006). In a genetics study using transgenic mice, Talpalar et al. (2013) revealed specific neurons related to the synchronization of left and right limbs in tetrapod locomotion.

Inspired by living things, robotics researchers have built various forms of

rhythmically coordinating artifacts with the aim to understand the mechanisms of movement coordination in animals. Mathematical models built in biological studies have been often useful to design robots. The majority has a number of oscillators, each of which connects with each other via electrical circuits (Kimura et al. 1999; Tsujita et al. 2001; Conradt & Varshavskaya 2003; Inoue et al. 2004; Lachat et al. 2006; Ijspeert et al. 2007; Crespi & Ijspeert 2008). On the other hand, some robotics studies have demonstrated the important coordinating role of physical properties independent of electricity. For example, four-limbed robots exhibited different locomotion patterns (e.g., trot, gallop) depending on the loading weight or the swing speed of each motor-driven limb although the limbs were physically connected without electrical circuit (Owaki et al. 2013; Owaki & Ishiguro 2018). A brittle-star-like robot designed by a similar concept was able to immediately change locomotion patterns owing to the unexpected loss of limbs (Kano et al. 2017). In these robots, the coordinated patterns of body parts are directly influenced by the morphology of the body. Such bio-inspired robots could then be a great platform for biologists to approach animals' mechanisms that are conceptually homologous to robots' ones. This means that, supposedly, such non-electrical coordinating networks are also utilized in animals in the form of non-neural networks.

In unicellular organisms without the nervous system, coordinated patterns can be altered depending on morphology. Takamatsu et al. (2000, 2001, 2004) made artificial structures composed of several wells connected by channels and filled each well with a cell of the true slime mold *Physarum polycephalum*. Each cell then fused with another cell in the channel and the cell portion in each well showed a rhythmic change in thickness. Two cell portions in a two-well structure showed a coordinated

pattern with antiphase synchronization (Takamatsu et al. 2000), whereas three cell portions in three-well structures showed other patterns, which can differ when wells were differently arranged (e.g., linear, circular) or sized (Takamatsu et al. 2001, 2004). This demonstrates that the body morphology of living things can directly affect movement coordination independent of neural activity.

In animals, however, it remains an issue of how body morphology affects neural and non-neural networks, i.e., movement coordination. This problem would arise from the lack of examples in which obviously different morphology results in obviously different coordinated patterns in animals.

1.2 Morphological variation and movement coordination

The morphology of animals is never identical even within a species. Body size is a representative that shows variation. As morphology differs, neural and non-neural networks must differ, making the coordinated patterns of movements different. By comparing the behavior of different congeneric species or subspecies, previous studies have suggested that morphological differences could cause differences in behavioral performance such as locomotion of lizards (Damme et al. 1998) and feeding posture of tits (Moreno & Carrascal 1993). For example, the way to increase the running speed differs between two subspecies of lizards; one increases stride length whereas the other increases stride frequency, which could result from a difference in limb morphology (Damme et al. 1998). At the intraspecific level, a study using frogs indicated that their jump distance increases significantly with hind-limb length adjusted by body mass (Tejedo et al. 2000). However, morphological variations targeted in these studies have

had difficulty in quantitative interpretation. In particular, body length is involved with other measurements continuously in three dimensions, and thus its meaning differs by the way of standardization considering other variables such as body size. Continuous variation makes it difficult to understand how a difference in morphology results in a difference in movement coordination.

Compared with the continuous cases, discrete morphological variation would result in more distinct differences in movement coordination. Discretely variable characters within species can be well recognized as the segment number of centipedes (Arthur 1999; Kettle & Arthur 2000; Arthur & Kettle 2001; Bonato et al. 2001) and the vertebral number of fish (Lindsey 1954) and amphibians (Lindsey 1966). Ackerly and Ward (2015, 2016) experimentally showed that the individuals of axolotls and zebrafish with more caudal vertebrae were able to turn more quickly in response to a threat. However, in these characters, it is still difficult to understand how each segment contributes to movement coordination so that the whole behavioral performance differs by its total number.

1.3 Number of rays in echinoderms

As mentioned above, the main problem in previous studies is a poor understanding of the relationship between morphological variation and movement coordination in animals. To address this issue, I focus on an intraspecific morphological variation that can be found in some species of echinoderms. This animal phylum (Echinodermata) shows a body plan with radial symmetry, as represented by the star shape of starfish. Because many species have five rays, it is often referred to as pentaradial symmetry.

However, some species vary the number of rays as the case of three- versus four-leaved clovers. It can be often recognized in the number of arms in asterozoans, i.e., starfish (class Asteroidea) and brittle stars (class Ophiuroidea). For example, *Patiria pectinifera*, a common starfish in Japanese waters, normally has five arms; however, a small number of individuals have four, six, or more arms (Kawase & Furukawa 2014). According to a field study on *Amphipholis squamata*, a small cosmopolitan brittle star, 99.71% of observed populations had five arms whereas 0.18% and 0.05% had four and six arms, respectively (Dupont & Mallefet 2002). In particular, variation in ray number is frequently found in fissiparous species, which undergo asexual reproduction by fission and regeneration (Boffi 1972; Mladenov et al. 1983; Mladenov & Emson 1984; Hotchkiss 2000). This indicates that the same genotype is capable of this morphological variation.

In the main nervous system of asterozoans, a radial nerve cord in each arm connects with each other via a circumoral nerve ring at the central disk (Smith 1937; Cobb & Stubbs 1981, 1982; Ghyoot et al. 1994; Bremaeker et al. 1997; Zueva et al. 2018). That is, this morphological variation must involve different numbers of branch points from the nerve ring to radial nerves, at which regional concentrations of neural cell bodies (recognizable as ganglia) would control some organs (Ghyoot et al. 1994). Many studies have indicated the important role of the nerve ring for inter-arm coordination in asteroids and ophiuroids (Romanes & Ewart 1881; Preyer 1887; Mangold 1909; Hopkins 1926; Diebschlag 1938; Arshavskii et al. 1976a,b; Clark et al. 2019; Kano et al. 2019a). Therefore, it is supposed that the variability of the number of branch points in the nerve ring affects the output patterns of coordinated movements.

The number of arms is equal to the number of interradii in the asterozoan body,

as each interradius represents a fan-shaped region partitioned by two nearest-neighboring arms. This means that interradial components (e.g., jaws, pairs of gonads, stomach pouches) have different numbers of repeats in accordance with the variation in arm number. In terms of geometry, the average angle of each interradius is 72 deg in a five-armed body but 60 deg in a six-armed body for instance. These differences would impact on non-neural coordinating networks as well.

However, there are few studies that compared behavior between individuals with different numbers of symmetric rays. Moore (1941) reported that a normal five-armed starfish of a *Patiria* species righted itself in 30 to 50 s—behavior after being upside down—whereas an apparently symmetric eight-armed individual usually required 5 to 10 min. Although this is a case study showing a bad influence of supernumerary arms upon movement coordination, the fact that the individual difference in arm number exists in many species implies that some extent of increase or decrease is not problematic for survival.

How can a coordinating network be flexible with the drastic morphological variation in body plan? In this study, I focus on the behavior of brittle stars given one advantage for observing locomotion; brittle stars dynamically flex arms to quickly propel the body, whereas starfish use a large number of tube feet arranged along arms to slowly move without largely changing the posture (Romanes & Ewart 1881; Preyer 1887). Brittle stars are thus expected to show coordinated patterns that could be measured obviously. Indeed, many studies have mentioned ophiuroid locomotion in the context of inter-arm coordination while targeting five-armed individuals with all arms intact or some arms severed (Romanes & Ewart 1881; Preyer 1887; Uexküll 1905; Glaser 1907; Arshavskii et al. 1976a,b; Astley 2012; Kano et al. 2017; Clark et al. 2019;

Kano et al. 2019a,b). Compared with the cases for other animals, it would be easier in brittle stars to understand how each numerically variable structure takes part in the movement coordination of the whole body.

1.4 Aims of this study

In the present study, I aim to examine how morphological variation affects coordinated movements and to suggest neural and non-neural networks that are flexible with the morphological variation. For this, I compare coordinated movements of brittle stars with different numbers of arms, and then identify a common coordinating rule among them on the assumption that their bodies comprise radially symmetric functional units, the number of which equals the number of arms. I hypothesize that each functional unit interacts only with nearest neighbors but the whole body moves in a coordinated manner regardless of the total number of units.

Two phenomena are investigated in the following chapters: “2. Locomotion of *Ophiactis brachyaspis*” and “3. Pumping of *Ophiarachna incrassata*.” In the former, I mainly focus on a neural network for the ophiuroid locomotion, a coordinated movement of arms. The latter is principally on a non-neural network for “pumping,” a coordinated movement of the ophiuroid disk, which will be firstly reported in this study.

2. Locomotion of *Ophiactis brachyaspis*

ABSTRUCT

Typical brittle stars have five radially symmetric arms that coordinate to move the body in a certain direction. However, some species have a variable number of arms, which is a unique trait since intact animals normally have a fixed number of limbs. How does a single species manage different numbers of appendages for adaptive locomotion? I herein describe locomotion in *Ophiactis brachyaspis* with four, five, six, and seven arms to propose a common rule for the behavior of brittle stars with different numbers of arms. For this, I mechanically stimulated each arm of individuals to analyze escape direction and arm movements. By gathering quantitative indices and employing Bayesian statistical modeling, I noted a pattern: regardless of the total number of arms, an anterior position emerges at one of the second neighboring arms to a mechanically stimulated arm, while arms adjacent to the anterior one synchronously work as left and right rowers. I propose a model in which an afferent signal runs clockwise or anticlockwise along the nerve ring while linearly counting how many arms it passes through. With this model, the question on how 'left and right' emerges in a radially symmetric body via a decentralized system is answered.

2.1 INTRODUCTION

Legged animals use appendages to move around on the ground. In most cases, intact adults of a species have a constant number of limbs; most mammals, for instance, have four limbs, whereas most insects have six. These species supposedly use a number-specific mechanism of locomotion. In contrast, in some species of brittle stars (Echinodermata: Ophiuroidea), some intact individuals have five appendages or less, whereas others have six or more (Fig. 1). This variability usually occurs in fissiparous species, which undergo asexual reproduction by fission and regeneration (Boffi 1972; Mladenov et al. 1983; Mladenov & Emson 1984).

Similar to typical echinoderms that show pentaradial symmetry, most ophiuroid species have five multi-jointed appendages called arms, which extend from the disk at the center of the animal. Previous studies have described arm movements in the locomotion of five-armed species in qualitative terms (Romanes & Ewart 1881; Preyer 1887; Uexküll 1905; Glaser 1907; Arshavskii et al. 1976a,b; Clark et al. 2019; Kano et al. 2019a,b) as well as in quantitative terms (Astley 2012; Kano et al. 2017). Several locomotion modes have been known to occur even in a single species. An often reported mode, referred to as "breast stroke" (Arshavskii et al. 1976a,b) or "rowing" (Astley 2012), is characterized by a leading arm facing forward, two side arms working as left and right rowers, and two back arms being dragged passively (Romanes & Ewart 1881; Preyer 1887; Glaser 1907; Arshavskii et al. 1976a,b; Astley 2012; Kano et al. 2017). Some studies have reported another locomotion mode, called "paddling" (Arshavskii et al. 1976a) or "reverse rowing" (Astley 2012), in which a backmost arm is dragged while the other four actively row (Preyer 1887; Uexküll 1905; Glaser 1907; Arshavskii et al. 1976a; Astley 2012). These

bilaterally coordinated movements enable the ophiuroid body to creep in a certain direction (Astley 2012). Nevertheless, since the role of each arm switches as the body changes moving direction (Arshavskii et al. 1976a; Astley 2012), brittle stars do not have consistent antero-posterior and left-right axes.

The ophiuroid nervous system mainly comprises a circumoral nerve ring in the disk and radial nerve cords running into each arm (Cobb & Stubbs 1981, 1982; Ghyoot et al. 1994; Bremaeker et al. 1997; Zueva et al. 2018). At each branch point to the radial nerve, the nerve ring has regional concentrations of neural cell bodies (i.e., ganglia) that control some organs (Ghyoot et al. 1994). Some behavioral studies have supported the essential role of the nerve ring in locomotion. For instance, menthol-anesthetic experiments described the nerve ring's function in initiating locomotion (Matsuzaka et al. 2017), whereas nerve cut experiments demonstrated its role in arm coordination (Mangold 1909; Diebschlag 1938; Arshavskii et al. 1976a,b; Clark et al. 2019; Kano et al. 2019a).

Although locomotion in common five-armed brittle stars and the morphological variability in some species have been studied in different contexts, no study has focused on locomotion of ophiuroids with different numbers of arms. Some studies have described locomotion with several severed arms (Arshavskii et al. 1976b; Kano et al. 2017; Matsuzaka et al. 2017; Clark et al. 2019; Kano et al. 2019b); however, in these cases, the pentameral architecture remained at the disk, including the nerve ring. There is a brief observation that three-armed halves after the fission of a six-armed fissiparous brittle star, *Ophiocomella ophiactoides*, scarcely move in the direction of the stumps and then increase the frequency to show this moving direction as they regenerate lost arms from the stumps (Mladenov et al. 1983); however, no detailed information about

arm-by-arm movements was mentioned and five-armed animals were not compared in this context. When the structural division differs at the center of the animal, the nerve ring must have a different number of branch points connecting it to the radial nerves, i.e., a different number of ganglia. Given the reported importance of the nerve ring in locomotion, this difference must result in a huge issue regarding the integration of the individual.

Therefore, the aims in this chapter are to understand how a species adapts its locomotion to a changeable number of limbs and network branches, and to propose a model for ophiuroid locomotion considering the varying number of radially symmetric arms. For this, I targeted four-, five-, six-, and seven-armed intact individuals of the fissiparous species *Ophiactis brachyaspis* H.L. CLARK, 1911 (Fig. 1). For probing into inter-arm communication, an aversive tactile stimulus was applied on one arm and the reactions of the other arms were observed. Although electrophysiological approaches are difficult in the small body of fissiparous ophiuroids, I expected each arm's movement to be a simple reflection of neural activity; therefore, external behavioral modeling will infer internal neural networks. My primary hypothesis was that brittle stars would have a decentralized nervous system, as suggested by previous studies (Cobb 1970; Moore & Cobb 1985; Cobb 1985). Matsuzaka et al. (2017), for instance, observed that unanesthetized arms carried food to the mouth in the wholly anesthetized disk; Kano et al. (2019a) cut the nerve ring at two points and observed that two- and three-armed portions within the five-armed body often crept oppositely to each other. To allow the variability of the total number of arms, each functional unit would neurally affect only the nearest-neighbor units while ignoring distant ones. In such a decentralized model, I expect a threat to an arm to make its both neighbors push toward the stimulus so that the

disk can escape in the direction opposite to the stimulus, as shown in Kano et al.'s (2019a) model.

I herein quantitatively described post-stimulus locomotion based on escape direction and arm movements, employing Bayesian estimation and model evaluation to understand their potential structures as reasonable distributions. The results indeed reinforced the support of a decentralized strategy in the ophiuroid body; however, contrary to my initial expectation, escape direction was not always the opposite of the stimulation direction. I here suggest the following model: a threat to an arm makes an afferent signal that asymmetrically dominates (in clockwise or anticlockwise direction) the nerve ring; in the same direction, the stimulated arm's *second* neighboring arm is highly probable to be the leading arm, with the leader's side arms working as left and right synchronous rowers. Thus, regardless of the total number of arms, ophiuroid locomotion shows a common anterior pattern, which could be positioned by linearly counting how many arms some signal passes in one direction along a circular pathway. I provide a unique idea of how a multi-directional body determines a movement direction.

2.2 MATERIALS AND METHODS

2.2.1 Animals

The fissiparous brittle star *Ophiactis brachyaspis* H.L. CLARK, 1911 (Fig. 1) was used. In nature, this species densely inhabits upper and lateral surfaces of rough rocks or adherent organisms such as sponges. Some of its arms lie in interstices while some rise from the substrate; suspension-feeding ophiuroids show this posture to capture particles (Warner 1971). Animals collected from Shirahama Aquarium, Kyoto University, were reared in a laboratory aquarium (450 × 450 × 450 mm) filled with artificial seawater at 25–28°C (TetraMarin Salt Pro, Tetra Japan Co, Tokyo, Japan; salinity, 32–35‰). Body size was 1.5–3.0 mm in disk diameter and 5–15 mm in arm length. Most specimens (approx. 70%) had six arms and others had five arms. One individual with four arms and another with seven arms, both quite rare, were obtained in this study.

2.2.2 Behavioral experiments

To investigate locomotion, 10 five-armed and 10 six-armed individuals were used. No arm was more than twice the length of the shortest arm in a specimen (c.f. Fig. 1). The four- and seven-armed individuals were also targeted. Each specimen was placed in a horizontal flat acrylic case (105 × 75 × 22 mm) filled with 100 mL of artificial seawater from the laboratory aquarium, with no strong light gradient and no strong current. Locomotion was recorded in aboral view using a digital camera (EOS8000D, Canon, Tokyo, Japan) with videos saved in MP4 format. Aversive tactile stimuli were applied to

arms to trigger escape behavior. In each trial, the very tip of an arm was manually tapped on both its lateral faces about four times with the sharp end of a toothpick. The next stimulus was applied at the anticlockwise neighboring arm after more than two minutes. This rotation order was repeated until all arms of each individual had been stimulated at least three times.

The locomotion for one minute after the disk began to move in response to each stimulus was extracted from long-term videos; the disk's movement generally started within ten seconds after stimulation. Per five- or six-armed individual, three trials that showed the longest moving distances of the disk were analyzed. For the four- and seven-armed individuals, the 15 trials with the longest moving distances were analyzed.

2.2.3 Measurements

To quantify temporal changes in body posture during locomotion, simple feature points that effectively outlined the ophiuroid movements were used. The stimulated arm in each trial was numbered 1, which was followed anticlockwise by the other arms; α is the index of arms (α = 1, 2, 3, 4, 5 in the five-armed instance). Using a semiautomatic tracking software Kinovea ver. 0.8.27 (http://www.kinovea.org/, accessed 4 December 2018), two coordinate points in each arm were traced at 10 f.p.s.: $P_\alpha(t) = (x_\alpha(t), y_\alpha(t))$—which indicates the attachment point of the α-th arm to the disk viewed aborally—and $P'_\alpha(t) = (x'_\alpha(t), y'_\alpha(t))$—which indicates the point at half the length of the α-th arm considering the range from the disk's center to the arm tip—at the t-th frame (Fig. 2; t = 1, 2, ..., 600). For $P'_\alpha(t)$, namely, the midpoint of each arm, I did not use the tip of the arm because it may rise or make casual movements irrelevant for locomotion, as indicated by Matsuzaka et al.

(2017). $P_{cent}(t)$ was defined as the center of gravity of all arm's basal points, $P_\alpha(t)$, and is similar to the center of the disk (Fig. 2).

Based on the above-mentioned points (two types of tracked points and one derivative point), I calculated several measurements that provided practical information. The α-th arm's length (L_α) was defined as the maximum length of the segment $P_\alpha(t)P'_\alpha(t)$ in the analyzed period; note that L_α was sampled in each trial, thus not accounting for the constant length of each arm. Moving distance (S) was measured as the length of $P_{cent}(1)P_{cent}(T)$, where T is the total number of frames, i.e., 600 (Fig. 2).

To understand in what direction the brittle stars escape after aversive stimulation, moving direction (Θ) was assessed as follows:

$$\Theta = \frac{1}{T}\sum_{t=1}^{T}\theta(t) \quad (1),$$

where $\theta(t)$ is the angle of the two segments $P_{cent}(1)P_{cent}(T)$ and $P_1(t)P_{cent}(t)$ (Figs 2, 3). Θ, which may be from −180 to 180 deg, is 0 deg when the disk moved in the direction opposite to the stimulated arm. A negative or positive value of Θ indicates that the track of the disk was inclined clockwise or anticlockwise, respectively, from the direction opposite to the stimulated arm. For statistics, the dummy variable Θ_{sign} was defined as

$$\Theta_{\mathrm{sign}} = \begin{cases} 0 & (-180 \le \Theta < 0) \\ 1 & (0 \le \Theta < 180) \end{cases} \quad (2).$$

Meanwhile, the movement of each arm during locomotion was calculated. In actively rowing arms, pushing backward was slower on the ground, while returning toward was faster off the ground. This directionality in arm angular velocity was used to quantify the degree to which each arm functions as a left or right rower. The angular velocity was obtained from arm angle in horizontal terms, informed by the defined points. The long segment $P_{cent}(t)P'_\alpha(t)$ during locomotion swung around the short one

$P_{cent}(t)P_{\alpha}(t)$, so each arm's angle at the t-th frame ($\varphi_{\alpha}(t)$) was defined as the angle formed by these two segments (Fig. 2). The arm angle $\varphi_{\alpha}(t)$ is negative or positive when $P_{cent}(t)P'_{\alpha}(t)$ was angled clockwise or anticlockwise, respectively, from $P_{cent}(t)P_{\alpha}(t)$. The arm angular velocity ($\omega_{\alpha}(t)$) was calculated from $\varphi_{\alpha}(t)$ with a five-point moving average method (window size 0.5 s), and then smoothened with a low-pass filter with the cut-off frequency of 1.0 Hz (Fig. 3). The filtered velocity $\omega_{\alpha}(t)$ was used to evaluate the degree of a leftward or rightward bias in arm movement, which is represented by B_{α} (named after "bias"; Fig. 3):

$$B_{\alpha} = \frac{1}{T}\sum_{t=1}^{T} \omega_{\alpha}(t)^2 \mathrm{sign}\big(\omega_{\alpha}(t)\big) \quad (3).$$

Assuming that a directional bias results from a speed difference between pushing and returning in each arm, B_{α} can be rephrased as each arm's tendency of being a left or right rower. A largely negative value of B_{α} represents that the α-th arm moved clockwise faster than anticlockwise, indicating that it slowly pushed leftward and returned fast rightward viewed proximally from the disk. In contrast, B_{α} is largely positive when the arm pushed rightward (clockwise). Its value is close to zero when the arm pushed leftward and rightward equally or was dragged without actively returning. Moreover, frequency components in the non-filtered $\omega_{\alpha}(t)$ of each arm were extracted using Fourier transforms. F_{α} was defined as the frequency at the peak amplitude in the α-th arm.

To understand how the arms synchronize with each other (i.e., synphase, no synchrony, or antiphase), the filtered velocity $\omega_{\alpha}(t)$ was used to calculate Kano et al.'s (2017) E_{ij}, namely, the degree of synchronization between two arms:

$$E_{\alpha\beta} = \frac{1}{T}\sum_{t=1}^{T} \omega_{\alpha}(t)\omega_{\beta}(t) \quad (4).$$

A negative or positive value of $E_{\alpha\beta}$ indicates that the movements of the α- and β-th arms

synchronized in the opposite (antiphase) or same direction (synphase), respectively. A value around zero represents that the two arms moved without synchrony or were static.

2.2.4 Statistical modeling

To capture a structure and correlation of measurements, I built multiple hypotheses in the form of probabilistic models regarding Θ, B_α, and $E_{\alpha\beta}$ (explained in this section), and later quantitatively compared how appropriate each hypothesis was using an information criterion (explained in "2.2.5 Bayesian inference and model evaluation").

Firstly, I hypothesized that brittle stars were likely to escape in one frequent direction (e.g., the direct opposite of the stimulus) or in two frequent directions. To examine a possible bimodality in moving direction, I assumed that Θ was subjected to a single von Mises distribution (f_{vM}, 'circular normal distribution'),

$$\Theta[n_{\mathrm{trial}}] \sim f_{\mathrm{vM}}(\mu_\Theta, \kappa_\Theta),\ -\pi \le \mu_\Theta \le \pi,\ \kappa_\Theta \ge 0 \quad (5),$$

or a mixture of two von Mises distributions,

$$\Theta[n_{\mathrm{trial}}] \sim \frac{1}{2} f_{\mathrm{vM}}(-\mu_\Theta, \kappa_\Theta) + \frac{1}{2} f_{\mathrm{vM}}(\mu_\Theta, \kappa_\Theta),\ -\pi \le \mu_\Theta \le \pi,\ \kappa_\Theta \ge 0 \quad (6).$$

Hereafter, n_{trial} takes one to the total number of trials, so that $\Theta[n_{\mathrm{trial}}]$ denotes the n_{trial}-th element of Θ. The parameters as random variables μ_Θ—converted to radians for modeling—and κ_Θ are analogous to the mean and the reciprocal of variance, respectively, in a normal distribution. For the mixed case, I assumed that the two distributions were symmetric to each other with respect to the position of 0 deg.

Secondly, I supposed that the leftward/rightward bias of each arm was associated with another factor such as arm length, moving direction, or some sort of individual difference. To understand what is largely related to a trial-by-trial variability of B_α, I

parametrized L_α, S, Θ, Θ_{sign}, and F_α each as an explanatory variable for B_α. A normal distribution $f_{\mathrm{norm}}(\mu, \sigma)$, where μ and σ respectively represent the mean and standard deviation (s.d.), was assumed as follows:

$$B_\alpha[n_{\mathrm{trial}}, \alpha] \sim f_{\mathrm{norm}}(\mu_{\mathrm{Bi}}[\alpha] + \mu_{\mathrm{Bs}}[\alpha]X, \sigma_{\mathrm{Bi}}[\alpha]),\ \sigma_{\mathrm{Bi}} \geq 0 \quad (7).$$

Here, μ_{Bi}, μ_{Bs}, and σ_{Bi} are arm-by-arm parameters and X is an explanatory variable to which $L_\alpha[n_{\mathrm{trial}}, \alpha]$, $S[n_{\mathrm{trial}}]$, $\Theta[n_{\mathrm{trial}}]$, $\Theta_{\mathrm{sign}}[n_{\mathrm{trial}}]$, or $F_\alpha[n_{\mathrm{trial}}, \alpha]$ is assigned. S, Θ, and Θ_{sign} were common values for all the arms in the same trial. The categorical index Θ_{sign} indicates whether B_α varies continuously by Θ or switches discretely by the sign of Θ. When Θ_{sign} stands for X, μ_{Bs} represents the means' difference between the negative and positive cases since this variable disappears if Θ_{sign} is zero ($-180 \leq \Theta < 0$) and appears if Θ_{sign} is one ($0 \leq \Theta < 180$). The model without the member $\mu_{\mathrm{Bs}}[\alpha]X$, i.e., without explanatory variables, was for comparison. In parallel, as for five- and six-armed animals, it was tested if B_α was well explained by individuality, namely, a quality made by some individual difference other than arm number. Consideration of individuality was given by the mean's intercept μ_{Bi}:

$$\mu_{\mathrm{Bi}}[n_{\mathrm{indiv}}, \alpha] \sim f_{\mathrm{norm}}(\mu_{\mathrm{B0}}[\alpha], \sigma_{\mathrm{B0}}),\ \sigma_{\mathrm{B0}} \geq 0 \quad (8),$$

$$B_\alpha[n_{\mathrm{trial}}, \alpha] \sim f_{\mathrm{norm}}(\mu_{\mathrm{Bi}}[i, \alpha] + \mu_{\mathrm{Bs}}[\alpha]X, \sigma_{\mathrm{Bi}}[\alpha]),\ \sigma_{\mathrm{Bi}} \geq 0 \quad (9),$$

where n_{indiv} takes one to the total number of individuals (i.e., 10) and the hyperparameters μ_{B0} and σ_{B0} are random variables. The parameter σ_{B0}, which is common in all arms, has a weakly informative prior as

$$\sigma_{\mathrm{B0}} \sim f_{\mathrm{t}}^{+}(3, 0, 20) \quad (10),$$

where f_t^+ denotes the half t distribution and the parenthetical parameters represent the degree of freedom (v), location (mean when $v > 1$), and scale (s.d. divided by $\sqrt{3}$ when $v = 3$), respectively.

Thirdly, the degree of synchronization between two arms was expected to be linked with moving distance or direction. Similarly to the models for B_α, a best explanatory variable for $E_{\alpha\beta}$ was explored in four- to seven-armed animals:

$$E_{\alpha\beta}[n_{\mathrm{trial}}, p] \sim f_{\mathrm{norm}}(\mu_{\mathrm{Ei}}[p] + \mu_{\mathrm{Es}}[p]X, \sigma_{\mathrm{Ei}}[p]),\ \sigma_{\mathrm{Ei}} \geq 0 \quad (11),$$

where p is the index of pairs, μ_{Ei}, μ_{Es}, and σ_{Ei} are pair-by-pair parameters, and the explanatory variable X takes $S[n_{\mathrm{trial}}]$, $\Theta[n_{\mathrm{trial}}]$, or $\Theta_{\mathrm{sign}}[n_{\mathrm{trial}}]$. A model without the explanatory member $\mu_{\mathrm{Es}}[p]X$ was also considered. No informative prior was set in all the parameters other than σ_{B0} (Equation 10).

2.2.5 Bayesian inference and model evaluation

The parameters were estimated by employing the Bayesian approach because most parameters in our model had posterior distributions that could not be approximated using any normal distribution; the maximum likelihood method gives less accurate inference than the Bayesian one in this case (Watanabe 2018). Especially, in singular models, which contain mixed distribution (c.f. Equation 6) or hierarchical parameters (c.f. Equations 8, 9) for instance, the maximum likelihood estimator often diverges or makes the generalization error very large (Watanabe 2009, 2010). The Bayesian inference is, however, sensitive to priors and statistical models made by scientists. To evaluate arbitrary pairs of priors and models, we used the widely applicable information criterion (WAIC), which is appropriate even for singular models (Watanabe 2009, 2010). Information presented in “2.3 Results” and “2.4 Discussion” is based on the models selected using WAIC.

Bayesian estimation was performed using the no-U-turn sampler (NUTS)

(Hoffman & Gelman 2014)—a variant of the Hamiltonian Monte Carlo (HMC) algorithm. In each sampling, 10,000 NUTS samples were obtained from four Markov chains, in each of which every 40th generation was sampled in 100,000 iterations after a warmup of 5,000, with the target acceptance rate of 0.8. Convergence of each parameter was checked by trace plots, the potential scale reduction factor $\hat{R} \leq 1.1$, and the effective sample size $\hat{n}_{eff} \geq 40$, i.e., at least 10 per chain (Gelman et al. 2013).

The resultant statements were developed according to better prediction models, which yielded smaller WAICs than the others considered. For comparison between models, I referred to the difference as

$$\Delta = 2N_{\mathrm{sample}}(W - W_{\mathrm{min}}) \quad (12),$$

where N_{sample} is the total number of measured samples (N_{sample} = 150 in the five-armed case; 30 trials multiplied by five arms); multiplication by $2N_{\mathrm{sample}}$ is for the AIC scaling (Gelman et al. 2013). W is the WAIC of a given model while W_{min} is the smallest WAIC among those of the proposed models; Δ is zero in a best performed model. For presenting figures, the posterior predictive distributions of Θ are shown based on the parameters' posterior distributions in a best model, each indicating a probability distribution which is expected to generate a random variable in a new trial. To visualize B_α and $E_{\alpha\beta}$ dependent on a best explanatory variable, the median of each posterior distribution was obtained under a model including the explanatory variable not only in the mean but also in the s.d.; Equation 7 or 9 was modified to

$$B_\alpha[n_{\mathrm{trial}}, \alpha] \sim f_{\mathrm{norm}}(\mu_{\mathrm{Bi}}[\alpha] + \mu_{\mathrm{Bs}}[\alpha]X, \exp(\sigma'_{\mathrm{Bi}}[\alpha] + \sigma'_{\mathrm{Bs}}[\alpha]X)) \quad (13),$$

while Equation 11 was replaced by

$$E_{\alpha\beta}[n_{\mathrm{trial}}, p] \sim f_{\mathrm{norm}}(\mu_{\mathrm{Ei}}[p] + \mu_{\mathrm{Es}}[p]X, \exp(\sigma'_{\mathrm{Ei}}[p] + \sigma'_{\mathrm{Es}}[p]X)) \quad (14).$$

Exponentiation in scale makes the s.d. positive while σ'_{Bi}, σ'_{Bs}, σ'_{Ei}, and σ'_{Es} are random

variables without constraints. I did not consider scale's explanatory variables when comparing WAICs because the Markov chain simulation failed to converge in many cases. Statistical computation was performed in the software environment R ver. 3.5.1 (R Core Team 2018), in which Stan codes were compiled and executed using the R package "rstan" (Stan Development Team 2018).

2.3 RESULTS

2.3.1 Escape direction

The post-stimulus moving direction Θ (Figs 2, 3; Equation 1 in "2.2.3 Measurements") is shown in Fig. 4 by dot plots. For all the four-, five-, six-, and seven-armed cases, based on the evaluation using WAIC, the results of Θ were better explained by the model assuming a mixture of two distributions than that assuming a single distribution (Table 1; note that a model with a smaller WAIC better predicts data than a model with a higher WAIC). In other words, it is likely that brittle stars showed two frequent escape directions rather than one. Compared to the four- and five-armed animals, the six- and seven-armed ones had larger differences of WAIC between one- and two-distribution models—represented by Δ in Table 1 (Equation 12). This indicates that the tendency for bimodality increased with number of arms. Following the better model in terms of WAIC, I hereafter show the results on the assumption of two frequent moving directions for all the cases.

The two peak locations were ±17, ±29, ±46, and ±70 deg in four-, five-, six, and seven-armed animals, respectively, informed by the posterior medians of means (μ_Θ) calculated separately for the negative and positive ranges. These estimated values indicate that the more arms a brittle star had, the further the two distributions of Θ were apart from each other (Fig. 4). In other words, the average moving direction of individuals with more arms was more inclined from the direction opposite to the stimulated arm. Predictive distribution of Θ indeed depicted this trend (Fig. 4).

2.3.2 Left or right rower

B_α—each arm's tendency of being a left or right rower (Figs 2, 3; Equation 3)—is schematized trial-by-trial in Figs 5–8. As for the five- and six-armed populations, no-individuality models were consistently better evaluated than their counterparts in which individuality was assigned to the mean of B_α (Table 1). I thus avoid mentioning individual difference within the same arm number.

Among L_α, S, Θ, Θ_{sign}, F_α, and no explanatory variable, the arm bias B_α in five-armed animals was best explained by the continuous moving direction Θ (Table 1). This means that the side in which each arm rowed was strongly associated with the direction to which the five-armed brittle stars escaped. As a similar result, the six- and seven-armed cases emphasized the importance of Θ_{sign} (Equation 2), the sign of moving direction in discrete terms. This indicates that the leftward/rightward bias of each arm could be categorized into two groups according to the range in which a six- or seven-armed brittle star escaped to the midline of the stimulated arm. In the four-armed specimen, the arm length L_α was chosen as a best explanatory variable although Θ showed a close performance, implying that each arm's movement bias changed with arm length and/or escape direction. Given the dominance of moving direction as a correlate of B_α, and also given Θ's bimodality (Fig. 4), I present the data of B_α separately by Θ_{sign}—in which side moving direction inclined from the midline of the stimulated arm. Two groups were herein defined based on whether the direction angled clockwise ($\Theta_{\mathrm{sign}} = 0$) or anticlockwise ($\Theta_{\mathrm{sign}} = 1$).

The Θ_{sign}-based grouping exhibited a common locomotion mode among four-, five-, six-, and seven-armed animals in regards to B_α's posterior means. The directional property of each arm could be explained by the number of arms counted from the

stimulated arm. Primarily, one of the *first* neighboring arms to the stimulated arm consistently took the largest or second largest $|B_\alpha|$—absolute values of posterior means (Figs 9–12A,C). This *first* arm corresponded to the anticlockwise neighbor of arm 1 when $\Theta_{\text{sign}} = 0$ (Figs 9–12A) and to the clockwise one when $\Theta_{\text{sign}} = 1$ (Figs 9–12C). The *second* neighbor from the stimulus—next to the *first* in the same direction—took the smallest or second smallest $|B_\alpha|$. Then, the *third* neighbor of the stimulus—next to the *second*—took the largest or second largest $|B_\alpha|$, which was opposite in sign to that of the *first*. One exception was the seven-armed specimen when $\Theta_{\text{sign}} = 0$ (Fig. 12A); the *second* (arm 3) and the *third* (arm 4) neighbors had the fourth smallest and the third largest $|B_\alpha|$, respectively, probably due to the outlying trial shown in row 1 of column 4 in Fig. 8. Replacing the ordinary cases' values with actual movements, the *first* actively pushed in the direction of the stimulated arm, while the *third* actively pushed oppositely to the *first*. These movements could make the *second* face forward, which indeed corresponded to the ranges of Θ in all the cases (Figs 9–12A,C).

2.3.3 Synchronization between two arms

The higher explanatory power of Θ_{sign} could also be applied to the instance of the degree of synchronization between the α- and β-th arms, $E_{\alpha\beta}$ (Equation 4), because the five-, six-, and seven-armed cases were each better explained by the model assuming Θ_{sign}'s effect than the others considered (Table 1). Thus, the synchronous movement of each arm with each other could be discretely grouped by in which side a brittle star escaped to the midline of the stimulated arm. In the four-armed animal, the model without an explanatory variable best performed while the presence of Θ or Θ_{sign} resulted in similar

performance, implying that arms synchronization was not strongly related to the measurements considered or was altered by the body's moving direction. Accenting the significance of Θ_{sign} as with B_α's situation, I here show the resultant values of the synchronization degree $E_{\alpha\beta}$ discretely by the sign of moving direction Θ.

A side-by-side comparison with the Θ_{sign}-based results of B_α showed us that the pair of the *first* and *third* rowers counting from the stimulated arm had the largest negative medians of $E_{\alpha\beta}$'s posterior means in most cases (Figs 9–12B,D). Although one exception was found in the seven-armed individual with $\Theta_{\mathrm{sign}} = 0$, the pair's value E_{24} leaned negatively as well (Fig. 12B). These values gave a quantitative indication that these two arms tended to simultaneously push in opposite directions, regardless of the number of arms.

2.4 DISCUSSION

In the present study, I newly described the post-stimulus locomotion of brittle stars based on the behavior of four-, five-, six-, and seven-armed intact individuals of a single species. For this purpose, by not stereotyping a discrete role of each arm, I introduced a quantitative index that represents each arm's tendency of being a left or right rower, namely B_{α}. Coupled with other supportive values, I propose the following common rule for specimens with different numbers of arms: brittle stars frequently travel in the direction of one of the second neighboring arms to the stimulated arm (Fig. 13). The proposed behavioral model thus presents a general scheme of how radially symmetric animals map 'left and right'—or 'front and back'—on its behavior via a decentralized control.

2.4.1 Locomotion modes

Previous quantitative studies using five-armed brittle stars have supported antiphase synchronization of two distant arms by assessing the stop and start timing of arm movements (Astley 2012) and by evaluating $E_{\alpha\beta}$ (Kano et al. 2017) as in the present study. This locomotion mode, which has been referred to as "breast stroke" or "rowing," is characterized by a leading arm and its side rowing arms (Romanes & Ewart 1881; Preyer 1887; Glaser 1907; Arshavskii et al. 1976a,b; Astley 2012; Kano et al. 2017; Clark et al. 2019; Kano et al. 2019b). The results regarding the five-armed specimens of *Ophiactis brachyaspis*, in which the rowing pair showed a high degree of antiphase synchronization (Fig. 9), agree with Kano et al.'s (2017) results for *Ophiarachna incrassata* based on the

commonly used index $E_{\alpha\beta}$. An important outcome of the present study is that even four-, six-, and seven-armed brittle stars have the triplet of left-front-right (Figs 10–12A,C), in which the left and right rowers tend to simultaneously push the ground backward (Figs 10–12B,D). This extension suggests that this locomotion mode is determined anteriorly, not laterally or posteriorly. However, the mechanism of synchronization of the left and right arms remains unknown, although I assume that it involves neural circuits that coordinate the anterior union.

The two back arms in the five-armed leading locomotion mode have been often interpreted as passively dragged ones (Romanes & Ewart 1881; Preyer 1887; Arshavskii et al. 1976a,b; Watanabe et al. 2011). However, the present study showed that these arms rather work as weaker rowers since their B_{α} values ranged either negatively or positively (Fig. 9A,C). In six- and seven-armed ophiuroids, the back arms following the two strong rowers similarly exhibited a rowing trend, whereas the backmost ones were usually neutral as to the leftward or rightward bias just like the leading arm (Figs 10A,C, 12A,C). Thus, more arms may become 'rowers,' especially in brittle stars with more arms.

Although "breast stroke" or "rowing" is a frequently reported locomotion mode in five-armed brittle stars, some studies have also described patterns in which there is no leading arm. One of these patterns is "paddling" or "reverse rowing," and it occurs when a backmost arm is dragged while the other four actively row (Preyer 1887; Uexküll 1905; Glaser 1907; Arshavskii et al. 1976a; Astley 2012). Such patterns without leading arms have been observed during free movement without experimental stimuli (Arshavskii et al. 1976a; Astley 2012) as well as during escape behavior for a short time (Yee et al. 1987). In my study using *Ophiactis brachyaspis*, each trial seldom showed such a non-leading pattern (Figs 5–8). Assuming that this species uses both locomotion modes, non-leading

patterns might be employed only for several seconds after stimuli. In this case, I may have overlooked or underestimated this phase in the present study since I uniformly analyzed one-minute duration after the beginning of the disk's movement. Still, considering the fixed period for which post-stimulus locomotion was herein quantified, it seems that locomotion using a leading arm is a more common mode in the intact individuals of *Ophiactis* species regardless of the number of arms.

2.4.2 Deciding moving direction

Since brittle stars show no consistent front in behavioral terms, as most echinoderms, every arm can be a leading arm. Astley (2012) described their turning behavior in a short-term series, which was performed by changing the roles of arms rather than by rotating their body axis. Regarding escape situations, previous studies have reported that brittle stars avoid open or bright spaces (Cowles 1910; Matsuzaka et al. 2017), predator extracts (Yee et al. 1987), and KCl solution as an aversive stimulus (Clark et al. 2019; Kano et al. 2019a). However, few studies have focused on how each arm reacts to such repellents and defines the direction of the movement of an individual. Since light and liquid diffuse in water, it is difficult to stimulate only a single target arm. Especially for small brittle stars such as *Ophiactis* species, tactile stimulation would perform effectively for the aim to understand how signals from a stimulated arm affect the movements of the other arms.

In this study, two quantitative indices calculated from the filtered angular velocity of arms—B_{α} and $E_{\alpha\beta}$—and one obtained from the original coordinate data—Θ—allowed us to visualize ophiuroid locomotion without contradiction (Figs 9–

12). By postulating each average of the two Θ_{sign}-based patterns as a representative, the numerical results indicated that the most frequent locomotion pattern after aversive tactile stimulation is the following: a leading arm emerges at the *second* neighbor of a stimulated arm, while side arms adjacent to the leader synchronously push backward, no matter how many arms a brittle star has. To perform this bilateral distribution with a high probability, it can be assumed that an afferent signal from an arm induces one of the *first* neighboring arms to be an active rower that pushes in the direction of the signaling arm, while the *second* neighboring arm is an inactive one and has a less important directional preference, and the *third* neighboring arm is active and pushes synchronously but oppositely to the *first*'s pushing (Fig. 13). Accordingly, the *second* arm faces forward while the *first*, *third*, and some rear arms work on the individuals both sides.

Kano et al. (2019a) proposed a model in which arm movements become potentially symmetric to aversive stimulation. I initially expected such a symmetric scheme to allow the animal to escape opposite to the stimulus. However, the present study demonstrates that the aversive signal makes an asymmetric effect on either direction (Fig. 13). In the currently proposed model, whether the clockwise or anticlockwise *second* arm becomes a leading arm depends on which direction the signal from the stimulated arm dominantly transfers. This either-or choice would be caused by asymmetry in a body posture or outer environment at the moment of stimulation. In particular, the bimodality in the seven-armed individual (Fig. 4D) could be an evidence that one individual determines either trial-by-trial. This mechanism of decision making should be further investigated. The apparent randomness might be beneficial in the escape behavior because it would be difficult for a predator to predict in which direction a brittle star will move. Moreover, this bimodality might give a brittle star an opportunity to select a

better escape way to hide itself quickly.

The present study provides important information on how behavioral direction is expressed in a body without antero-posterior and left-right axes. Even when the individual's body is round, some direction-making signal could transfer linearly in one direction at a local view on the circumference (Fig. 13), just like a wave on a string or neural transmission in the spinal cord. If brittle stars indeed use this strategy, the number of segments with identical function in the pathway is not important.

2.4.3 Neural and non-neural networks

The inter-arm connection depicted in Fig. 13 is recognizable as the circumoral nerve ring, i.e., the main portion of the nervous system that runs in the disk. This correspondence is indicated by its orbital morphology as well as previous studies that support the importance of the nerve ring in locomotion (Mangold 1909; Diebschlag 1938; Arshavskii et al. 1976a,b; Matsuzaka et al. 2017; Clark et al. 2019; Kano et al. 2019a). Although it is difficult to measure neural activity in the small body of *Ophiactis* species, such an internal neural network can be suggested from behavioral modeling based on external observation. Given the simplicity of the ophiuroid nervous system, it can be assumed that the movement of each arm directly reflects neural activity in each unit, which could also be explained by a couple of neurons. For instance, the observed locomotion can be used for testing "neuron ring" models (Suzuki et al. 1971; Matsuoka 1985) and the functioning of circularly arranged neurons. The unique variability of fissiparous brittle stars allows us to test the function of different numbers of neurons, connecting theoretical biology and experimental biology.

Besides the crucial role of neural networks, Kano et al. (2017) identified the ophiuroids' ability to immediately change their locomotion patterns after losing some arms and built an ophiuroid-like robot that imitated the animal's adaptive locomotion via a local feedback without pre-programmed control. Other robotics studies have also suggested the importance of 'physical' interactions in movement coordination which is independent of electrical circuits (Owaki et al. 2013; Owaki & Ishiguro 2017). The results of these studies indicate that four- to seven-armed individuals are not likely to employ different central control systems while counting the total number of arms. Each functional unit—e.g., each arm and each branch of the nerve ring—would refer to the states of its nearest-neighbor units while ignoring distant ones; nevertheless, a coordinated pattern casually arises at a level of individual, no matter how many units they own. In this perspective, the worse performance of the individuality-assuming model (Table 1) implies that an important structural hierarchy for a brittle star might be each unit rather than an individual body. A trial-by-trial variability in moving direction and other indices (Figs 5–8) might reflect the influence of non-neural networks formed by physical properties such as arms' posture at each moment, although a circular neural network would chiefly design the average orientation, in which the stimulated arm's *second* neighbor faces forward (Fig. 13).

Except for the unexpected escape direction in the more-armed cases, the resultant concept fits my initial hypothesis in terms of a decentralized design. The high independence among body sectors may have contributed to ophiuroid evolution and allowed variability in appendage number. This may be a reason why some species such as *Ophiactis brachyaspis* have acquired fissiparity, being capable of drastic morphological changes in a life cycle while retaining its locomotive ability. The unique 'non-brained'

strategy of fissiparous brittle stars may serve as a base for a highly flexible design in robotics. More specifically, multi-directional robots may imitate the ophiuroid model's high mobility in every horizontal direction while promptly reacting to external stimuli.

2.4.4 Functional difference by morphological variation

Under the proposed model shown in Fig. 13, brittle stars with more arms have a higher risk of approaching a threat such as a predator. If the front is placed ideally around the *second* neighboring arm from the stimulus, four-, five-, six-, and seven-armed animals will respectively show 0, 36, 60, and 77 deg in average $|\Theta|$. In fact, the estimation from the measured data was similar—17, 29, 46, and 70 deg, respectively—, and trials in which moving direction inclined toward the stimulated arm ($90 < |\Theta| \leq 180$) were more frequent as the tested body had more arms: 0/15, 1/30, 3/30, and 5/15, respectively (Fig. 4). Although this behavior as a response to a threat is considered less adaptive, an evolutionary background would explain it. It has been proposed that primitive ophiuroids showed pentaradial symmetry (Paul & Smith 1984; Sumrall & Wray 2007), implying that brittle stars had developed a locomotion mechanism which worked optimally for the five-armed body. Some exceptional individuals in arm number, at least the four-, six-, and seven-armed bodies, probably have kept following this initial plan without vital issues. Meanwhile, escape direction may be more or less inclined as a side effect, and the minority of four- and seven-armed ones might be a reflection of some inconvenience in control mechanism or its resultant behavior.

2.4.5 Dynamics and muscle anatomy

I analyzed the ophiuroid locomotion based on the direction of horizontal movements (yaw). This simple approach with kinematics resolved a clear difference and similarity of locomotion between individuals with different arm numbers (Figs 4, 9–12), satisfying the aim of this study. Although the low-cost method that supported valid results is a strength of this study, a deeper understanding of their locomotion process would require the consideration of forces as the cause of movements. Such an approach with dynamics has been done in previous studies that built robots based on the behavioral observations—including the lateral view for vertical movements (pitch)—of intact or damaged five-armed brittle stars (Kano et al. 2017, 2019b). In particular, Kano et al. (2019b) considered the muscle anatomy of ophiuroid arms, in which two muscle series in the oral side and two muscle series in the aboral side connect adjacent arm segments (Wilkie 1978). The rowing movement of an arm would involve the four muscle series' contraction that continuously differs along the proximo-distal axis of the arm. Kano et al. (2019b) simulated the ophiuroid locomotion on the assumption that each arm's pushing movement is served by oral contraction in one side of the proximal segments and aboral contraction in the other side of the distal segments. If this is applied to the model of Fig. 13, the proximal segments of the *first* arm, for example, would have the contraction of oral muscle series in the side close to the stimulated arm. It has been indicated that the middle part is often on the ground in a rowing arm and is thus responsible for propulsion (Matsuzaka et al. 2017; Kano et al. 2019b). In this context, the tracking of each arm's midpoint $P'_{\alpha}(t)$ in the present study (c.f. Fig. 2) could reasonably capture a perspective of dynamics.

2.4.6 Limitations

Although I conducted behavioral experiments on a flat acrylic surface, *Ophiactis* brittle stars typically inhabit rough rocky surfaces. They lay some arms in interstices while raising some arms from the substrate; suspension-feeding ophiuroids commonly show this posture (Warner 1971). In their habitats, ophiuroids' arms may not be chiefly used for locomotion, and escaping direction may depend on their posture at each moment. Thus, the proposed model should be further tested using ophiuroid species that live on bottom surfaces and have active locomotion, such as *Ophiura* and *Ophiarachna*. However, these non-fissiparous brittle stars have low variability in number of arms, and thus a large number of five-armed specimens should be investigated to analyze their potential bimodality in locomotion.

Intact individuals with other than five or six arms are rare even among fissiparous brittle stars. Although I observed only one specimen with four arms and one with seven arms, I believe that the bias caused by individual selection was not large given the good performance of the non-individuality model in five- and six-armed individuals' movements. Still, ideally, rare cases should also be further investigated using a large sample size to consolidate the proposed model.

Finally, the fissiparous brittle stars collected in the same aquarium might be clones resulting from the asexual reproduction of a single individual. It is possible that locomotion is affected by a genotype, and this may reflect the high support of the non-individuality model. Further studies sampling individuals from different localities would solve this issue.

3. Pumping of *Ophiarachna incrassata*

ABSTRUCT

Coordinated patterns in the locomotion of brittle stars have been characterized with some tendency in a period. However, a high degree of freedom in arm movements makes it difficult to understand coordinating networks along the time series. To address this issue, I herein report a simple rhythmic coordinated movement in the green brittle star *Ophiarachna incrassata*. I found this animal moved the disk's five radially symmetric parts (interradii; fan-shaped regions partitioned by adjacent arms) in well-ordered unsynchronized patterns. Based on externally observable movements and anatomical features, I built a mathematical model in which body fluid flows between the five body parts to explain the coordinated pattern without considering neural interactions between the parts. Changing the number of the parts from five to six, I simulated a synchronized pattern, which was demonstrated also by an individual with six symmetric interradii. The proposed model suggests a different number in morphology makes a different fluid flow, leading to a different synchronization pattern in the animal.

3.1 INTRODUCTION

The locomotion of brittle stars with a variable number of arms would be a good model system to understand how animals manage coordinated movements in accordance with body morphology. Some tendency of arm movements, such as the degree of synchrony, can be captured in a fixed period, as done in previous studies (Kano et al. 2017; Clark et al. 2019) and in the previous chapter "2. Locomotion of *Ophiactis brachyaspis*." However, ophiuroid locomotion has a high degree of freedom since it involves the flexible movements of several (e.g., five) arms, each of which has numerous joints. In the presence of many casual movements, it is difficult to trace the coordination along the time series; how the movements of an arm follow those of another is not clearly resolved. The high degree of freedom in movement also complicates the interpretation of coordinating networks, especially non-neural ones, which would be affected by an unspecified number of physical properties.

To break this impasse, I herein report a simple rhythmic coordinated movement in the central disk of the green brittle star *Ophiarachna incrassata* (LAMARCK, 1816), which mostly has five arms. The observed movement comprised several cycles of shrinkage and expansion in the five interradii (symmetric fan-shaped parts in the disk partitioned by five arms) and frequently occurred after feeding (Fig. 14). Individuals that were kept without feeding even for a week never showed the movement, implying a relationship with digestion. I termed this rhythmic movement "pumping" because it was reminiscent of pumps. The movements between the five interradii were regularly ordered without synchronization. According to a mathematical model built based on external observation and anatomical investigation (Figs 15–18), these coordinated patterns can be easily explained by a non-neural network, i.e., physical properties

without considering neural interactions between interradii. I then changed the number of interradii in the model, referring to the fact that brittle stars sometimes have individual difference in the number of arms, namely, the number of interradii. Simulation after changing from five to six interradii made synchronized movements between the interradii (Fig. 19). I finally obtained a six-armed individual, which demonstrated the well-synchronized movements (Fig. 20). Therefore, pumping will provide a model system to understand the role of morphology in movement coordination utilized in actual animals.

3.2 MATERIALS AND METHODS

3.2.1 Animals

Intact adult individuals of the green brittle star *Ophiarachna incrassata* (LAMARCK, 1816) were used in this study. They were obtained commercially and reared in laboratory aquariums (450 × 450 × 450 mm) filled with artificial seawater at 25–28°C (TetraMarin Salt Pro, Tetra Japan Co, Tokyo, Japan; salinity, 32–35‰). The disks ranged 2–5 cm in diameter and mostly had five symmetric arms. I also obtained an individual that had six arms with a 4-cm disk in diameter.

3.2.2 Behavioral observation

All animals were fed with dried krill (Tetra Krill-E, Tetra Japan Co, Tokyo, Japan). Once they detected the food, their arms captured it and carried it to their mouths. After a while, their disks start moving rhythmically—pumping. The long-term behavior of four randomly selected five-armed individuals and one six-armed animal were recorded using a time-lapse camera (TCL200, Brinno, Taipei, Taiwan). The short-term rhythmic movements, pumping, of two randomly selected five-armed animals and the one six-armed animal were recorded three times for each from the aboral side with a video camera (EOS8000D, Canon, Tokyo, Japan) in small acrylic cases. Successfully recorded movements were analyzed using a semiautomatic tracking software Kinovea ver. 0.8.15 (http://www.kinovea.org/, accessed 30 April 2018) at 10 f.p.s.

3.2.3 Anatomical observation

The internal structure of the disk during pumping was investigated with X-ray micro-computed tomography (micro-CT). Cryogenic liquid ethanol was used to instantly freeze animals at the moment of pumping. For this purpose, a living animal was put in a styrofoam box (127 × 157 × 100 mm) with 200 mL of artificial seawater and then fed with a dried krill. While pumping was observed, 200 mL of −80°C ethanol was poured onto the disk so that the animal kept a momentary shape with partial expansion and shrinkage (Fig. 15). The frozen samples (two individuals) was post-fixed with Bouin's solution for fixing internal tissue with less shrinkage. To observe a normal form of internal structure, another specimen was anesthetized in a solution of 3% $MgCl_2$ for an hour at room temperature, and then fixed in Bouin's fixation without the cryogenic process. Both types of specimens in Bouin's solution were stored at 4°C for a few days.

For *tert*-butyl alcohol replacement to keep the original morphology as possible (Inoué & Osatake 1988), specimens after Bouin's fixation were dehydrated with ethanol series (70%, 80%, and 90%) for two days each. They were then stained with 1% iodine diluted in ethanol for three days at 3°C to enhance the contrast of tissues in later X-ray exposure (Metscher 2009). They were rinsed with 100% ethanol for a day at room temperature and then moved into *tert*-butyl alcohol liquidized with a water bath above 40°C. After immersion in *tert*-butyl alcohol for a day twice at 26°C, specimens were superficially dried on wiping papers for several seconds and then put at −20°C for 10 min to instantly freeze *tert*-butyl alcohol. They were freeze-dried by using a vacuum evaporator (PX-52, Yamato Ltd., Japan) with a cold alcohol trap (H2SO5, AS ONE, Japan). All chemicals were purchased from Kanto Chemical Co. (Tokyo, Japan).

Specimens were scanned on an X-ray micro-CT system (inspeXio, SMX-100CT,

Shimadzu Corporation, Kyoto, Japan), in which the X-ray source was operated at 75 kV and 40 μA. Scanned images were reconstructed and rendered by using VGStudio MAX ver. 2.2.6 (Volume Graphics, Heidelberg, Germany) with the voxel size of 10–50 μm.

Because a large space inside the disk of brittle stars is occupied by a digestive tract (Schechter & Lucero 1968; Pentreath 1971; Deschuyteneer & Jangoux 1978), the surface view of the cavity was visualized with segmentation using Amira ver. 2019.1 (Thermo Scientific, Waltham, USA). In scanned images, a boundary with contrasting X-ray absorptivity can be recognized as a surface of some structure. The internal lining of the digestive tract beginning from the mouth was traced. The surface of gut contents, which were recognizable as highly absorptive areas inside the digestive cavity, was also traced.

3.2.4 Mathematical modeling

Mathematical models using differential equations to explain the time series of the rhythmic movements were built based on the external and internal observations of five-armed specimens. Assumptions and parameters are presented in "3.3.3 Modeling and simulation."

3.3 RESULTS

3.3.1 Behavior of five-armed brittle stars

The rhythmic movement in the five-armed individuals of the green brittle star, pumping, was frequently observed with an interval of 21 ± 10 min (mean ± s.d. in measured data; four individuals) after feeding (Fig. 14A). Each continuously moving phase, termed "pumping phase," started with a closing of the mouth and genital slits on the oral side of the disk. The whole contraction of the disk was immediately followed by a series of shrinkage and expansion in interradii. Five-armed individuals produced a pumping phase for 57 ± 12 s (two individuals; six pumping phases), in which each of the five interradii repeated 3–5 cycles of the movements. Based on the radius of the interradii in the aboral view, each cycle comprised a shrinking period for 5.9 ± 1.0 s and an expanding period for 6.5 ± 0.8 s at the beginning of the pumping phase (Fig. 14B). These phases gradually became longer to 7.6 ± 1.0 and 8.1 ± 0.9 s respectively at the end. Meanwhile, the amplitude of the movements gradually became smaller. Each expanding period included two increasing stages in radius; the first longer one was recognized as an increase in the volume of the interradii, while the second shorter one was apparently ascribed to change in the form of the interradii.

Numbered from 1 to 5 anticlockwise in the aboral view, the interradii regularly moved in the unsynchronized sequence of 1-3-5-2-4 (Fig. 14B–G) or 1-4-2-5-3 repetitively; a cycle in one of the five interradii was followed by that in either of two distant ones with 2.2 ± 0.5 s delayed. Here, a rotation of two expanding portions could be recognized in the disk (Fig. 14C–G), implying that body fluid flows

inside the disk. Fluid in an interradius seemed to transfer mostly to one of the nearest-neighbor interradii. In the 1-3-5-2-4 pattern, an expanding portion—a mass of fluid—was recognizable in the repeating sequence of 1-5-4-3-2; the expanding portion at the 1st interradius moved to the 5th (Fig. 14C–E), and after a short delay, the other expanding portion at the 3rd moved to the 2nd (Fig. 14D–F). Oppositely, the 1-4-2-5-3 pattern seemed to make fluid flow in the sequence of 1-2-3-4-5 repetitively.

The two types of sequences were observed in the same individual although a continuous pumping phase underwent either one consistently. The initially shrinking interradius was not always identical. At the end of the pumping phase, the mouth and genital slits slowly opened, so that the disk became relaxed as usual (Fig. 14B).

3.3.2 Anatomy

X-ray micro-CT imaging showed the internal morphology of the disk in terms of non-pumping (Fig. 16) and pumping forms (Figs 17, 18). In the non-pumping specimen fixed after anesthesia, five arm skeletons seemed radially symmetric (Fig. 16A) and weakly partitioned the disk's internal cavities including the stomach (Fig. 16B). The digestive tract was well imaged from the mouth to the stomach by segmenting its inner lining (Fig. 16C–E). The stomach comprised five larger interradial pouches and five smaller radial pouches (Fig. 16C). As separations between the pouches seemed not remarkable, the stomach was recognizable as a single sac that occupied a large space inside the disk. The stomach was plain in the aboral side (Fig. 16C,D) but well wrinkled in the oral side (Fig. 16E). Radial pouches were restricted in the aboral side by arm skeletal plates and thus flatter than interradial pouches, which extended until near the

oral wall (Fig. 16D). The oral space at the center contained a jaw apparatus and its peripheral organs, which would include the circumoral nerve ring and the water vascular system and narrowed the stomach in the aboral side (Fig. 16A,B). In this specimen, large pieces of food (given krill) were observed at the aboral side across radial and interradial pouches and at the oral side of an interradial pouch (Fig. 16C–E).

The specimens frozen during pumping kept shrinking and expanding interradii well (Figs, 17A, 18). In the digestive tract, a constriction between the mouth and the stomach was easily defined (Fig. 17B; see the esophagus "e"). The stomach wall was smoothly fitted to the distorted body wall with less obvious folding (Figs 17C, 18). Expansions were more remarkable in interradial pouches than in radial pouches apparently due to the lying of arm skeletal plates (Fig. 17D). The oral surface likewise showed an entire extension, in which wrinkle structures were barely found (Fig. 17E). The cavity between the body and stomach walls (perivisceral coelom) appeared to be narrowly limited (Figs 17B,D, 18). Interradii that expanded in the pumping specimens (Fig. 18A,B) were similar to those in the anesthetized specimen (Fig. 16) in morphology, implying that expansion occurs at relaxed interradii (Fig. 18A,B) while shrinking interradii actively contract (Fig. 18C,D). The contraction of muscles (or connective tissues as found in sea lilies; Birenheide & Motokawa 1996; Motokawa et al. 2004) could be assumed in the body or stomach wall. The muscle contraction of the body wall is more likely given the large and rapid morphological change of the body surface; the stomach wall seems too tender to achieve this change.

3.3.3 Modeling and simulation

A mathematical model was built to explain the relationship between the pumping pattern and morphology. Previous theoretical studies explained how rhythmic outputs depend on neural networks in which a certain number of neurons constituted a ring (Kling & Székely 1968; Suzuki et al. 1971; Matsuoka 1985). These models were inspired in contexts irrelevant to pumping; nevertheless, they demonstrated that pumping-like rhythmic patterns were generated among five neurons which laterally inhibited each other. Although brittle stars possess a nerve ring in the disk (Cobb & Stubbs 1982), it is unclear whether they utilize such a neural network. I suppose that their simple nervous system is insufficient to coordinate the dynamic movements of pumping, and rather physical properties of their body have a dominant effect. I thus constructed a phenomenological model simply focusing on the external morphological change in interradii and the internal morphological structure of the disk, independent of neural interactions between interradii.

Based on the anatomical investigation, I assumed that fluid flows that are crucial for pumping occur inside the stomach, which is weakly partitioned into five symmetric interradial spaces by arm skeletons (Figs 16, 17). The fluid volume in the i-th interradius at the time t is represented by $u_i(t)$; the index i takes 1 to N anticlockwise—$N = 5$ in the case of five interradii. The total volume of fluid $\sum_{i=1}^{N} u_i(t)$ is constant in this situation, given that the mouth, esophagus, and genital slits closed during pumping (Figs 15A, 17B). I also considered the pressure at the i-th interradius, namely, $p_i(t)$. Because it was difficult to experimentally determine the fluid property in the connection between the interradii, theoretical approaches to the fluid dynamics would be formidable attempts. However, with a rough estimation, the fluid would flow

in a similar manner to Hagen-Poiseuille flow (Sutera & Skalak 1993). Accordingly, I assumed that the flow rate between the interradii is proportional to the pressure gradient; the time evolution of $u_i(t)$ is described as

$$\frac{\mathrm{d}u_i}{\mathrm{d}t} = \sum_{j=1}^{N} C_{ij}\left(p_j - p_i\right) \quad (15).$$

C_{ij} represents the ease with which fluid flows between the i-th and j-th interradii. It would be greater when the internal opening between the interradii is shorter and wider. I assumed that the value of C_{ij} for the nearest neighbors is larger than that for the others, based on the geometric closeness as well as the observation that expansion in an interradius seemed to transfer mostly into a neighboring one.

The pressure $p_i(t)$ is given by the sum of the pressure generated by elastic membrane surrounding the interradius $p_{\mathrm{elas},i}(t)$, and the pressure actively generated by muscles $p_{\mathrm{mus},i}(t)$ (c.f. Fig. 18), namely,

$$p_i = p_{\mathrm{elas},i} + p_{\mathrm{mus},i} \quad (16).$$

I supposed that $p_{\mathrm{elas},i}(t)$ increases as the volume of fluid increases, and it is thus given by

$$p_{\mathrm{elas},i} = a{u_i}^m \quad (17),$$

where a represents the stiffness of the membrane. Considering that pumping makes a minute change in volume in a small size, $m = 1$ for simplicity. Meanwhile, I assumed that $p_{\mathrm{mus},i}(t)$ is given by

$$\tau \frac{\mathrm{d}p_{\mathrm{mus},i}}{\mathrm{d}t} = \bar{p}_{\mathrm{mus},i} - p_{\mathrm{mus},i} \quad (18),$$

where τ denotes the time constant. The target pressure of muscles $p_{\mathrm{mus},i}$ is described as

$$\bar{p}_{\mathrm{mus},i} = \begin{cases} p_0 \text{ (shrinking period)} \\ 0 \text{ (expanding period)} \end{cases} \quad (19),$$

where p_0 is a positive constant. The passive expanding period switches to the active shrinking period when u_i exceeds $u_{\max}$, while the shrinking period switches to the

expanding period when u_i falls below $u_{\min}$.

At the beginning of the pumping phase, an interradius starts to shrink casually. Since gut contents asymmetrically distributed in the stomach (c.f. Fig. 16C–E), I took the initial condition that one of the interradius has a larger volume than the others and is in the shrinking period, while the others are in the expanding period: $(u_1, p_1) = (u_{\text{high}}, au_{\text{high}}{}^m + p_0)$ and $(u_i, p_i) = (u_{\text{low}} + \varepsilon\xi_i, a(u_{\text{low}} + \varepsilon\xi_i)^m)$ for $i = 2, N$. Here, $u_{\text{high}} > u_{\text{low}}$, ε is a positive constant, and ξ_i takes a random value within [−1.0, 1.0].

Simulation results showed that the interradii regularly moved in the unsynchronized sequence of 1-3-5-2-4 with suitably chosen parameters (Fig. 19A): $a = 1$, $p_0 = 20$, $u_{\max} = 0.5$, $u_{\min} = 0.1$, $\tau = 0.2$, $C_{ij} = 0.2$ for nearest neighbors, $C_{ij} = 0.02$ for the others, $u_{\text{high}} = 1$, $u_{\text{low}} = 0.2$, and $\varepsilon = 0.05$; after $t = 4$, p_0 was decreased constantly so that it became zero at $t = 6$. The 1-4-2-5-3 pattern was also observed depending on the noise ξ_i. The numerical simulations thus supported the experimental results well.

I here focused on the fact that brittle stars sometimes have individual difference in the number of arms, namely, the number of interradii. One familiar example is the existence of six-armed animals in species that normally have five arms. Therefore, I simply changed the number of interradii from five to six, in which a different synchronization pattern was found in the model simulation (Fig. 19B). Numbered from 1 to 6, the interradii moved in the synchronized sequence of 1, 3, and 5 together and then 2, 4, and 6 together repetitively; synchronized cycles in three distant ones followed that in the other three.

After $t = 4$, I assumed muscle fatigue to decrease p_0 gradually to zero, given the observation that the disk became relaxed at the end of the pumping phase. In both the cases of $N = 5$ and 6, the cycles became longer and finally the oscillation vanished in the

same way as in the experiments (Fig. 19).

3.3.4 Behavior of a six-armed brittle star

I then obtained a six-armed individual with six symmetric interradii, in which pumping was also observed. The interval between pumping phases was 19 ± 2 min (one individual) after feeding (Fig. 20A). Each pumping phase continued for 39 ± 14 s (one individual; three pumping phases) with the six interradii each repeating 2–4 cycles. The duration of shrinking and expanding periods at the beginning of the pumping phase was 5.4 ± 0.8 and 6.7 ± 0.6 s respectively, which became 5.7 ± 0.8 and 8.6 ± 1.6 s, respectively, at the end. The movements in the interradii were well-synchronized as occurs in the simulation (Fig. 20B–E).

3.4 DISCUSSION

Based on the observation of pumping in the five-armed individuals of the green brittle star (Fig. 14B–G), I built a phenomenological model in which a non-neural network robustly generated the rhythmic movement in five interradii (Fig. 19A), which is also applicable to the case of six interradii (Figs 19B, 20B–E). The correspondence to the real phenomena in the two morphological types suggests that the modeled network is likely to coordinate the animal's movement, independent of neural interactions between interradii.

3.4.1 Non-neural network and different synchrony

The difference in synchrony between five- and six-armed bodies can be explained by the volume and pressure. Fluid connections between non-nearest-neighbor interradii can be ignored in this model; the output patterns were consistent even with $C_{ij} = 0$ for distant ones. For the case of $N = 5$, the 1st interradius initially pushes its fluid into the 2nd and 5th ones, and then the 2nd and 5th push it into the 3rd and 4th, respectively. At the beginning, the difference between u_3 and u_4 is small. However, for example, when u_3 exceeds the upper threshold ($u_{\max}$) and u_4 is still in the expanding period, the fluid flows from the shrinking 3rd to the expanding 4th. The difference between u_3 and u_4 increases rapidly (by $t = 2$ in Fig. 19), so that each interradius in five-armed individuals makes an asymmetric flow into either neighbor (Fig. 21A). The direction of the rotation—1-5-4-3-2 or 1-2-3-4-5—depends on the initial perturbation, which is realized by the noise ξ_i in the model. In the absence of the noise, the pair 2nd-5th and the pair 3rd-4th each synchronized in simulation. For the case of $N = 6$, the fluid flows starting

from the 1st interradius are propagated anticlockwise (1-2-3-4) and clockwise (1-6-5-4) and collide with each other at the 4th one. After the collision, the 4th pushes the fluid back to the 3rd and 5th. If the 3rd has a larger volume than the 5th, the pressure of the 3rd is also larger than that of the 5th based on Equation 17 because both are in the expanding period. Then following Equation 15, more fluid flows into the 5th than into the 3rd. As a result, u_3 and u_5 come to synchronize; the 4th acts as a buffer to eliminate the difference between u_3 and u_5. This mechanism causes each interradius in six-armed individuals to make symmetric flows into both neighbors (Fig. 21B), dividing the interradii into two well-synchronized groups (Fig. 20C,E).

3.4.2 Function and its difference by morphological variation

Given the occurrence of pumping related with feeding (Figs 14A, 20A), this coordinated movement would be a digestive activity. In many animals including humans, food transfers from the mouth to the anus in one direction; the linear structure guarantees that nutrients are absorbed point by point. On the other hand, the digestive cavity of brittle stars has neither unidirectional tracts nor the anus (Austin 1966; Schechter & Lucero 1968; Pentreath 1971), so a piece might easily stick to a dead end (c.f. Fig. 16C–E). Transformation of the stomach by pumping would give more opportunities to displace the piece and spread a nutritious flow. This strategy would be effective in large-sized species, in which gut contents travel longer distances piece by piece. Therefore, although we used the single species *Ophiarachna incrassata*, other large brittle stars are supposed to exhibit pumping in a similar manner. I never observed pumping in *Ophiactis brachyaspis*, the small species examined in the

locomotion chapter (Fig. 1), as expected in this functional perspective.

Suppose pumping functions in a digestive process, the difference in synchrony can be referred to different intestinal movements (Fig. 21). The interradii of five-armed individuals can make a traveling wave (Fig. 21A), which resembles peristaltic motion for transporting liquid matter in intestine (Umetani & Inou 1985) (Fig. 21C). On the other hand, the six-armed interradii can bring a stationary wave (Fig. 21B) as recognized in segmental motion for mixing solid matter (Umetani & Inou 1985) (Fig. 21D). Accordingly, the morphological variation in arm number could cause a functional difference, which might be a reason why the majority of extant brittle stars show pentaradial symmetry, not hexaradial symmetry. Investigation into the function of pumping and comparative analyses of the efficiency between five- and six-armed bodies would provide more concrete understanding.

Although I have focused on the stomach fluid thus far, another candidate for the role of pumping is to translocate the perivisceral coelomic fluid to the entire body including arms. In the body of brittle stars, the perivisceral coelom extends from the disk to the aboral and lateral portions of arms (Austin 1966). The transformation of the disk would more or less push the fluid, which contains nutrients absorbed via the digestive tract, to the cavity of arms. In this case, functional difference between five- and six-armed animals would be of minor importance. However, in comparison with other echinoderm classes—asteroids, echinoids, and holothuroids—, ophiuroids have a smaller volume of the perivisceral coelom in relation to the body size and show no recognizable change in the diameter of arms during movement (Austin 1966). The narrow cavity and rigid skeletal armor of their arms would make much less significant flows, compared to the large opening and flexible covering of the stomach.

3.4.3 Other rhythmic movements in the disk

Respiratory behavior “bursal ventilation” is another reported cyclic movement in the disk of brittle stars (Gislén 1924; Austin 1966). I suppose that bursal ventilation and pumping are not homologous based on three reasons. Firstly, I also observed long-term cyclic shrinkages of the whole disk in *Ophiarachna incrassata*, which can be referred to as bursal ventilation and recognized as a different phenomenon from pumping. Secondly, bursal ventilation is described as a movement that makes a flow through bursal slits, whereas pumping seems not to achieve this purpose since the slits tightly close during pumping (c.f. Fig. 15A). Thirdly, bursal ventilation is a phenomenon in which the entire disk—all the interradii—moves uniformly, whereas the movement timing of each interradius differs during pumping. Nevertheless, it is possible that the long-term occurrence of pumping is related to the cycle of bursal ventilation.

3.4.4 Central pattern generator

Previous studies explaining rhythmic movements in animals have built mathematical models assuming the existence of autonomous oscillatory activity of pacemaker neurons, so-called central pattern generators (CPGs) (Stein 1978; Delcomyn 1980; Grillner et al. 1981; Marder & Calabrese 1996; Grillner 2006). Robotics studies focusing on physical properties have also employed the idea of CPGs, as designed in each limb for locomotion (Owaki et al. 2013; Owaki & Ishiguro 2017) and in intestinal wall for peristalsis (Kano et al. 2013). Even apart from animals, protoplasmic movement in the true slime mold has inspired physicists and robotics researchers to build mathematical

models related to the number of circularly arranged oscillators (Takamatsu et al. 2000, 2001, 2004; Umedachi et al. 2013). Although this unicellular organism has no nervous system, these models have instead assumed spatially distributed biochemical oscillators in the body, which are similar to CPGs in concept. In this perspective, the proposed model without explicit CPGs in the present study helps us begin to understand how biological movements take advantage of morphology, independent of spontaneous oscillation in neurons or biochemicals.

3.4.5 Model validity and neural network

In this chapter, the validity of the proposed non-neural network based on five-armed brittle stars was post-assessed by its predictability of an additional observation, i.e., the correspondence between the predicted and actual movements in the six-armed case. However, this does not mean that the involvement of neural networks for coordinating pumping has been rejected. Indeed, the important role of neural networks has been indicated in the coordination of intestinal movements (Umetani & Inou 1985)—a phenomenon comparable to pumping. Moreover, what a series of pumping phases periodically occurred in the long run (Figs 14A, 20A) can suggest that long-term cycles of some matter such as neurotransmitters contribute to the initiation of pumping phases. The balance of neural and non-neural networks in realizing the whole phenomenon of pumping should be investigated in further studies.

3.4.6 Limitation

I observed only one individual with six interradii in this chapter, due to its extreme

rarity in *Ophiarachna incrassata*. I suppose the collected six-armed animal had a simple addition of a symmetric functional unit, given the model in which the same set of parameters only with different node numbers well fit the real patterns of both five- and six-armed animals. Still, ideally, the six-armed case should be further investigated using a large sample size to show the consistent difference in the synchrony of pumping.

4. GENERAL DISCUSSION

This study presented neural and non-neural networks underlying coordinated movements that are flexible with a drastic morphological variation in animals, which would be realized by a highly decentralized control system at the level of an individual.

4.1 Modeling of coordinating networks

In "2. Locomotion of *Ophiactis brachyaspis*," I analyzed the post-stimulus locomotion of four-, five-, six-, and seven-armed individuals regarding the tendency in a fixed period, and then proposed a neural network that can exist in brittle stars (Fig. 13). In "3. Pumping of *Ophiarachna incrassata*," I analyzed the rhythmic movements of the disk of five- and six-armed individuals along the time series, and then proposed a non-neural network that brittle stars might employ (Fig. 21A,B).

This study presented a unique methodology to infer networks responsible for movement coordination, taking advantage of morphological variation in the arm number of brittle stars (c.f. Fig. 1). Investigation only into five-armed ophiuroids would not highlight these network models. For example, what an animal often escapes oppositely to a threat is one easily hypothesized scheme (Domenici et al. 2011). Some studies have indeed suggested an opposite escape scheme of five-armed brittle stars (Yee et al. 1987; Kano et al. 2019a). When escape direction has bimodality especially with close peak locations, a small sample size would not resolve this structure. Even if a study with a large sample size supported that five-armed ophiuroids frequently escaped in the direction around one of the two distant arms to the stimulated arm (c.f. Figs 4A, 9A,C), it would be unclear whether the distant arm faced forward because it was the nearest

arm to the stimulus's opposite or it was two neighboring arm to the stimulated arm, unless neural activity is directly recorded. In the case of pumping, various models with a wide range of parameters would make simulations similar to the five-armed patterns (Fig. 19A), whereas sets that commonly explain the five- and six-armed cases would be limited (Fig. 19A,B). The situation in which the number of functional units obviously differs gave an evaluation of the proposed models even based on the external observation of individuals without operation such as experimental cuts.

4.2 Decentralized autonomous system

In the ophiuroid body, the central disk would be an important place in which each arm or interradius interacts with each other. Although it is disk-shaped, networks that coordinate body movements would be circularly arranged (c.f. Figs 13, 21A,B), just as a rosary. That is, the whole individual body can show a coordinated movement even if each of the functional units, the number of which equals the number of arms, affects the nearest-neighbor functional units. This interaction can be not only neural one (Fig. 13), but also one without neural activity, as shown with the fluid flow model for pumping (Fig. 21A,B).

This strategy would be involved with a decentralized autonomous system, which comprises uniform components that can interact with each other to perform global functions without integrated monitor or control (Ihara & Mori 1984). Accordingly, this system accommodates, for example, resistance to partial failure or damage, smooth adaptation to environmental changes by local feedback, and flexibility to the number of components (Corfmat & Morse 1976; Ihara & Mori 1984). An easily

understandable example of decentralized autonomous systems in animals would be the synchronous behavior of a group of fish, birds, or humans (Vicsek 2001). Although each individual must recognize neither distant individuals nor the entire form of the mass, the group naturally behaves as if it is a huge individual; an enormous cost would be required if one director commanded individual-by-individual behavior to achieve the same group performance. A scheme similar to the group case would be utilized in the echinoderm body, in which each symmetric functional unit acts as an individual to casually move the whole body as a group.

The decentralized autonomous system at the level of an individual would enable easy multiplication and reduction of body units within animal species. Supposedly, echinoderms as well as other animals share the important role of nearest-neighbor interactions. For example, centipedes also show wide-ranged intraspecific variation in the number of segments (Arthur 1999; Kettle & Arthur 2000; Arthur & Kettle 2001; Bonato et al. 2001). Their undulatory locomotion can be explained by a coordinating network with nearest-neighbor interactions of segments (Yasui et al. 2017). As in centipedes, most bilaterians have a linear arrangement of metameric units, in which one terminal is always cephalized, i.e., neurally centralized. The whole body would eventually behave under the command of the center to a moderate extent. In this context, echinoderms' coordinating networks proposed in the present study are unique in terms of the circular arrangement of metameric units. One region hardly comes to centralization since the ring has no end. Thus, the degree of decentralization could be higher in echinoderms than the other bilaterians. The movement coordination of this radially symmetric scheme might require less support of the costly nervous system and rather take advantage of the body morphology itself,

making coordinating networks highly flexible with morphological variation. This might be a reason why apparently drastic morphological difference such as radial symmetry with four to seven repeats is not fetal and can coexist in an echinoderm species.

4.3 Constraint of morphological variation

Although morphological variation in the ray number of asterozoans (starfish and brittle stars) is acceptable to some degree, they must have a constraint in variable range. In the specimens of *Ophiactis brachyaspis* observed in the locomotion chapter, most had six arms, others had five arms, only one had four arms, and another had seven arms. In *Ophiarachna incrassata* for the pumping chapter, all specimens had five arms except for one that had six arms. Also given other reports (Hotchkiss 1979, 2000), each asterozoan species must have an optimal range of the number of rays.

In Moore's (1941) case study on a *Patiria* starfish, which normally has five arms, an eight-armed individual without operation sometimes behaved like a specimen with two cuts in the nerve ring. One such observation was that opposite sides of the starfish walked in opposite directions, showing a lack of integration in locomotion (Moore 1941). This indicates that a determinant of the 'anterior' pattern (c.f. Fig. 13) emerges at one point on the circular network of a normal five-armed individual, whereas the aberrant eight-armed body is unexpectedly wide so that the 'anterior' determinant can emerge at two points. Nevertheless, other asteroid species which normally have more than eight arms show coordinated locomotion (Kjerskog-Agersborg 1918; Kjerschow-Agersborg 1922). Thus, it is supposed that the exclusive range of the 'anterior' determinant differs by species, which would reflect some difference in neural

networks coordinating locomotion.

In this view, it cannot be guaranteed that the proposed models are applied to a body with a ray number that was not examined in the present study. An eight-armed individual of *Ophiactis brachyaspis* might show the conflict with doubled 'anterior' patterns, while a seven-armed individual of *Ophiarachna incrassata* might lose the regularity of pumping at all. No collection of these specimens might result from low survivability due to such dysfunction.

4.4 Benefit of morphological variation

When morphological variation is drastic as found in asterozoans' ray number, it would result in behavioral variation, which might be beneficial to maintain populations. The present study indicates that brittle stars with different numbers of arms show different distributions of escape direction in locomotion (Fig. 4) and different waving manners in pumping (Fig. 21). One of the variable phenotypes could be beneficial under a specific environmental pressure. For example, if an invasive predator has a range of vision or moving direction that is good at capturing a prey that escapes in the direction opposite to the predator, six- and seven-armed brittle stars, which show lower frequencies of the opposite escape (Fig. 4B,D), would have a more survivability than four- and five-armed ones, which often escape oppositely (Fig. 4A,C). In this case, this ophiuroid population would be able to avoid mass mortality even with a single genotype. Regarding pumping, if the body of preys in an area becomes solid, stationary-wave pumping in six-armed brittle stars (Fig. 21B), which could work better for mixing and breaking solid contents in the gut (c.f. Fig. 21D), might be more beneficial than traveling-wave pumping in

five-armed brittle stars (Fig. 21A), which could be rather effective for liquid transportation (c.f. Fig. 21C).

Intraspecific behavioral variation caused by drastic morphological variation might drive speciation. Where an environment brings a significant advantage for one phenotype and a serious disadvantage for another phenotype for a long term, the former would be selected and might become a new species in this area with a different range of morphological variation. This speciation process might partially contribute to the great diversity in the ray number of asterozoans (Hotchkiss 2000) as well as other animals' cases such as the segment number of centipedes (Arthur 1999; Bonato et al. 2003; Minelli et al. 2009).

4.5 Robotics application

Decentralized autonomous systems have been implemented in robotics designs to benefit from the strong points mentioned in "4.2 Decentralized autonomous system." Many have been inspired by the behavior of animals or even by that of unicellular organisms, such as flocking (Shen et al. 2004; Kim et al. 2006; Halloy et al. 2007; Antoniou et al. 2009; Ge et al. 2012; Vásárhelyi et al. 2014) and locomotion (Cruse et al. 2006; Jakimovski et al. 2010; Umedachi et al. 2013; Kano & Ishiguro 2013). Regarding brittle stars, Kano et al. (2017, 2019b) have built locomotive robots with decentralized control schemes; moving direction was manually determined in these but Kano et al. (2019a) performed computer simulations in which brittle stars escaped oppositely to aversive stimulation in a self-organized manner. These ophiuroid designs, however, have commonly had a pentameral architecture at the center.

In this series, the present study would contribute to the generalization of the number of functional units (e.g., legged components) and advances the decentralized autonomous nature in robotics design. The proposed models for locomotion and pumping would be specifically applicable to radially symmetric robots that allow self-organized addition and subtraction of their identical functional units (Fig. 22). The automatic change in the number of working units would enable a quick replacement of damaged units and a flexible switching of function in response to environments. For example, following the proposed model of locomotion (Fig. 13), a multi-directional robot with more arms would automatically show a trajectory with sharper turns, just as the escape of the seven-armed brittle star (Fig. 4D). In the pumping model, a fluid system with an odd number of pumping units would circulate contents, whereas that with an even number would mix contents, given the different waving patterns and the function of intestinal movements (Umetani & Inou 1985) (Fig. 21). Because relevant parameters (e.g., the exclusive range of the 'anterior' determinant in locomotion) could be regulated in robotics, the proposed models would inspire various ways to automatically change coordinated patterns according to the purpose.

Gaps between the movements of bio-inspired robots and those of inspiring animals will then highlight what factor is missed in the understanding of coordinating networks in the animals. For example, if a fluid system imitating the ophiuroid body fails to reproduce the pumping patterns, some unrealistic aspect of the proposed model will be revealed to motivate us to re-examine the animal at the specific aspect. Such a cross-disciplinary approach, referred to as robotics-inspired biology (Gravish & Lauder 2018), will improve biological insights with innovative ways.

REFERENCES

Ackerly KL & Ward AB (2015) Linking vertebral number to performance of aquatic escape responses in the axolotl (*Ambystoma mexicanum*). *Zoology* **118**, 394–402.

Ackerly KL & Ward AB (2016) How temperature-induced variation in musculoskeletal anatomy affects escape performance and survival of zebrafish (*Danio rerio*). *J Exp Zool A* **325**, 25–40.

Alexander RM (1984) The gaits of bipedal and quadrupedal animals. *Int J Robot Res* **3**, 49–59.

Antoniou P, Pitsillides A, Blackwell T, & Engelbrecht A (2009) Employing the flocking behavior of birds for controlling congestion in autonomous decentralized networks. *Proc IEEE Cong Evol Comp* **11**, 1753–1761.

Arshavskii YI, Kashin SM, Litvinova NM, Orlovskii GN, & Fel'dman AG (1976a) Types of locomotion in ophiurans. *Neurophysiology* **8**, 398−404.

Arshavskii YI, Kashin SM, Litvinova NM, Orlovskii GN, & Fel'dman AG (1976b) Coordination of arm movement during locomotion in ophiurans. *Neurophysiology* **8**, 404−410.

Arthur W (1999) Variable segment number in centipedes: population genetics meets evolutionary developmental biology. *Evol Dev* **1**, 62–69.

Arthur W & Kettle C (2001) Geographic patterning of variation in segment number in geophilomorph centipedes: clines and speciation. *Evol Dev* **3**, 34−40.

Astley HC (2012) Getting around when you're round: quantitative analysis of the locomotion of the blunt-spined brittle star, *Ophiocoma echinata*. *J Exp Biol* **215**, 1923–1929.

Austin WC (1966) Feeding mechanisms, digestive tracts and circulatory systems in the ophiuroids: *Ophiothrix spiculata* le Conte, 1851 and *Ophiura luetkeni* (Lyman, 1860). Stanford University Press. (dissertation)

Birenheide R & Motokawa T (1996) Contractile connective tissue in crinoids. *Biol Bull* **191**, 1–4.

Boffi E (1972) Ecological aspects of ophiuroids from the phytal of SW Atlantic Ocean warm waters. *Mar Biol* **15**, 316–328.

Bonato L, Foddai D, & Minelli A (2001) Increase by duplication and loss of invariance of segment number in the centipede *Mecistocephalus microporus* (Chilopoda, Geophilomorpha, Mecistocephalidae). *Ital J Zool* **68**, 345–352.

Bonato L, Foddai D, & Minelli A (2003) Evolutionary trends and patterns in centipede segment number based on a cladistic analysis of Mecistocephalidae (Chilopoda: Geophilomorpha). *Syst Entomol* **28**, 539–579.

Bremaeker ND, Deheyn D, Thorndyke MC, Baguet F, & Mallefet J (1997) Localization of S1- and S2-like immunoreactivity in the nervous system of the brittle star *Amphipholis squamata* (Delle Chiaje 1828). *Proc Royal Soc B* **264**, 667–674.

Calabrese RL (1977) The neural control of alternate heartbeat coordination states in the leech, *Hirudo*

medicinalis. *J Comp Physiol* **122**, 111–143.

Clark EG, Kanauchi D, Kano T, Aonuma H, Briggs DE, & Ishiguro A (2019) The function of the ophiuroid nerve ring: how a decentralized nervous system controls coordinated locomotion. *J Exp Biol* **222**, 192104.

Cobb JLS (1970) The significance of the radial nerve cords in asteroids and echinoids. *Z Zellforsch Mik Ana* **108**, 457–474.

Cobb JL (1985) The neurobiology of the ectoneural/hyponeural synaptic connection in an echinoderm. *Biol Bull* **168**, 432–446.

Cobb JL & Stubbs TR (1981) The giant neurone system in ophiuroids I: the general morphology of the radial nerve cords and circumoral nerve ring. *Cell Tissue Res* **219**, 197–207.

Cobb JL & Stubbs TR (1982) The giant neurone system in ophiuroids III: the detailed connections of the circumoral nerve ring. *Cell Tissue Res* **226**, 675–687.

Conradt J & Varshavskaya P (2003) Distributed central pattern generator control for a serpentine robot. *Proc Int Conf Artif Neural Netw* **13**, 338–341.

Corfmat JP & Morse AS (1976) Decentralized control of linear multivariable systems. *Automatica* **12**, 479–495.

Cowles RP (1910) Stimuli produced by light and by contact with solid walls as factors in the behavior of ophiuroids. *J Exp Zool* **9**, 387–416.

Crespi A & Ijspeert AJ (2008) Online optimization of swimming and crawling in an amphibious snake robot. *Proc IEEE Trans Robot* **24**, 75–87.

Cruse H, Dürr V, & Schmitz J (2006) Insect walking is based on a decentralized architecture revealing a simple and robust controller. *Philos Trans Royal Soc A* **365**, 221–250.

Damme RV, Aerts P, & Vanhooydonck B (1998) Variation in morphology, gait characteristics and speed of locomotion in two populations of lizards. *Biol J Linn Soc* **63**, 409–427.

Delcomyn F (1980) Neural basis of rhythmic behavior in animals. *Science* **210**, 492–498.

Deschuyteneer M & Jangoux M (1978) Comportement alimentaire et structures digestives d'*Ophioderma longicauda* (Retzius) (Echinodermata, Ophiuroidea). *Ann I Oceanogr* **54**, 127–138.

Diebschlag E (1938) Ganzheitliches verhalten und lernen bei echinodermen. *Z Vergl Physiol* **25**, 612–654.

Domenici P, Blagburn JM, & Bacon JP (2011) Animal escapology I: theoretical issues and emerging trends in escape trajectories. *J Exp Biol* **214**, 2463–2473.

Dupont S & Mallefet J (2002) Abnormal forms in the brittle-star *Amphipholis squamata*: a field study. *J Mar Biol Assoc UK* **82**, 491–493.

Ekeberg Ö & Grillner S (1999) Simulations of neuromuscular control in lamprey swimming. *Philos Trans Royal Soc B* **354**, 895–902.

Ge F, Wei Z, Lu Y, Tian Y, & Li L (2012) Decentralized coordination of autonomous swarms inspired by chaotic behavior of ants. *Nonlin Dynam* **70**, 571–584.

Gelman A, Stern HS, Carlin JB, Dunson DB, Vehtari A, & Rubin DB (2013) *Bayesian Data Analysis*. 3rd edition. Florida, USA: CRC Press.

Ghyoot M, Cobb JLS, & Thorndyke MC (1994) Localization of neuropeptides in the nervous system of the brittle star *Ophiura ophiura*. *Philos Trans Royal Soc B* **346**, 433–444.

Gislén T (1924) Echinoderm studies. *Zool Bidr Upps* **9**, 1–316.

Glaser OC (1907) Movement and problem solving in *Ophiura brevispina*. *J Exp Zool* **4**, 203–220.

Gravish N & Lauder GV (2018) Robotics-inspired biology. *J Exp Biol* **221**, 138438.

Grillner S (2006) Biological pattern generation: the cellular and computational logic of networks in motion. *Neuron* **52**, 751–766.

Grillner S, McClellan A, & Perret C (1981) Entrainment of the spinal pattern generators for swimming by mechano-sensitive elements in the lamprey spinal cord *in vitro*. *Brain Res* **217**, 380–386.

Grillner S, Wallen P, Brodin L, & Lansner A (1991) Neuronal network generating locomotor behavior in lamprey: circuitry, transmitters, membrane properties, and simulation. *Ann Rev Neurosci* **14**, 169–199.

Halloy J, Sempo G, Caprari G, Rivault C, Asadpour M, Tâche F, Saïd I, Durier V, Canonge S, Amé JM, Detrain C. Correll N, Martinoli A, Mondada F, Siegwart R, & Deneubourg JL (2007) Social integration of robots into groups of cockroaches to control self-organized choices. *Science* **318**, 1155–1158.

Hill AA, Masino MA, & Calabrese RL (2002) Model of intersegmental coordination in the leech heartbeat neuronal network. *J Neurophysiol* **87**, 1586–1602.

Hodgkin AL & Huxley AF (1952) A quantitative description of membrane current and its application to conduction and excitation in nerve. *J Physiol* **117**, 500–544.

Hoffman MD & Gelman A (2014) The No-U-Turn sampler: adaptively setting path lengths in Hamiltonian Monte Carlo. *J Mach Learn Res* **15**, 1593–1623.

Hopkins AE (1926) On the physiology of the central nervous system in the starfish, *Asterias tenuispina*. *J Exp Zool* **46**, 263–275.

Hotchkiss FHC (1979) Case studies in the teratology of starfish. *Proc Acad Nat Sci Phila* **131**, 139–157.

Hotchkiss FHC (2000) On the number of rays in starfish. *Am Zool* **40**, 340–354.

Ihara H & Mori K (1984) Autonomous decentralized computer control systems. *Computer* **8**, 57–66.

Ijspeert AJ, Crespi A, Ryczko D, & Cabelguen JM (2007) From swimming to walking with a salamander robot driven by a spinal cord model. *Science* **315**, 1416–1420.

Inoue K, Ma S, & Jin C (2004) Neural oscillator network-based controller for meandering locomotion of snake-like robots. *Proc IEEE Int Conf Robot Autom* **21**, 5064–5069.

Inoué T & Osatake H (1988) A new drying method of biological specimens for scanning electron microscopy: the t-butyl alcohol freeze-drying method. *Arch Histol Cytol* **51**, 53–59.

Jakimovski B, Meyer B, & Maehle E (2010) Firefly flashing synchronization as inspiration for

self-synchronization of walking robot gait patterns using a decentralized robot control architecture. *Proc Int Conf Archit Comput Syst* **23**, 61–72.

Kano T & Ishiguro A (2013) Obstacles are beneficial to me!: scaffold-based locomotion of a snake-like robot using decentralized control. *Proc IEEE/RSJ Int Conf Intell Robot Syst* **26**, 3273–3278.

Kano T, Kawakatsu T, & Ishiguro A (2013) Generating situation-dependent behavior: decentralized control of multi-functional intestine-like robot that can transport and mix contents. *J Robot Mech* **25**, 871–876.

Kano T, Sato E, Ono T, Aonuma H, Matsuzaka Y, & Ishiguro A (2017) A brittle star-like robot capable of immediately adapting to unexpected physical damage. *Royal Soc Open Sci* **4**, 171200.

Kano T, Kanauchi D, Aonuma H, Clark EG, & Ishiguro A (2019a) Decentralized control mechanism for determination of moving direction in brittle stars with penta-radially symmetric body. *Front Neurorobot* **13**, 66.

Kano T, Kanauchi D, Ono T, Aonuma H, & Ishiguro A (2019b) Flexible coordination of flexible limbs: decentralized control scheme for inter-and intra-limb coordination in brittle stars' locomotion. *Front Neurorobot* **13**, 104.

Kawase O & Furukawa R (2014) Regional difference of ray number variation in a starfish, *Patiria pectinifera*. *Ann Rep Premed Sci Dokkyo Med Univ* **3**, 49–52.

Kettle C & Arthur W (2000) Latitudinal cline in segment number in an arthropod species, *Strigamia maritima*. *Proc Royal Soc B* **267**, 1393–1397.

Kim DH, Wang H, & Shin S (2006) Decentralized control of autonomous swarm systems using artificial potential functions: analytical design guidelines. *J Intell Robot Syst* **45**, 369–394.

Kimura H, Akiyama S, & Sakurama K (1999) Realization of dynamic walking and running of the quadruped using neural oscillator. *Auton Robot* **7**, 247–258.

Kjerschow-Agersborg HP (1922) The relation of the madreporite to the physiological anterior end in the twenty-rayed starfish, *Pycnopodia helianthoides* (Stimpson). *Biol Bull* **42**, 202–215.

Kjerskog-Agersborg HP (1918) Bilateral tendencies and habits in the twenty-rayed starfish *Pycnopodia helienthoides* (Stimpson). *Biol Bull* **35**, 232–254.

Kling U & Székely G (1968) Simulation of rhythmic nervous activities. *Kybernetik* **5**, 89–103.

Lachat D, Crespi A, & Ijspeert AJ (2006) Boxybot: a swimming and crawling fish robot controlled by a central pattern generator. *Proc IEEE/RAS-EMBS Int Conf Biomed Robot Biomechatron* **1**, 643–648.

Lindsey CC (1954) Temperature-controlled meristic variation in the paradise fish *Macropodus operculars* (L.). *Can J Zool* **32**, 87–98.

Lindsey CC (1966) Temperature-controlled meristic variation in the salamander *Ambystoma gracile*. *Nature* **209**, 1152–1153.

Mangold E (1909) Studien zur physiologie des nervensystems der echinodermen. *Pflug Arch Eur J Phy* **126**,

371–406.

Marder E & Calabrese RL (1996) Principles of rhythmic motor pattern generation. *Physiol Rev* **76**, 687–717.

Matsuoka K (1985) Sustained oscillations generated by mutually inhibiting neurons with adaptation. *Biol Cybern* **52**, 367–376.

Matsuzaka Y, Sato E, Kano T, Aonuma H, & Ishiguro A (2017) Non-centralized and functionally localized nervous system of ophiuroids: evidence from topical anesthetic experiments. *Biol Open* **6**, 425–438.

Metscher BD (2009) MicroCT for comparative morphology: simple staining methods allow high-contrast 3D imaging of diverse non-mineralized animal tissues. *BMC Physiol* **9**, 11.

Minelli A, Chagas-Júnior A, & Edgecombe GD (2009) Saltational evolution of trunk segment number in centipedes. *Evol Dev* **11**, 318–322.

Mladenov PV & Emson RH (1984) Divide and broadcast: sexual reproduction in the West Indian brittle star *Ophiocomella ophiactoides* and its relationship to fissiparity. *Mar Biol* **81**, 273–282.

Mladenov PV, Emson RH, Colpit LV, & Wilkie IC (1983) Asexual reproduction in the West Indian brittle star *Ophiocomella ophiactoides* (H.L. Clark) (Echinodermata: Ophiuroidea). *J Exp Mar Biol Ecol* **72**, 1–23.

Moore AR (1941) Dysfunction in righting and locomotion in a starfish (*Patiria*) with supernumerary rays. *J Comp Psychol* **32**, 483–487.

Moore A & Cobb JLS (1985) Neurophysiological studies on photic responses in *Ophiura ophiura*. *Comp Biochem Physiol A* **80**, 11–16.

Moreno E & Carrascal LM (1993) Leg morphology and feeding postures in four Parus species: an experimental ecomorphological approach. *Ecology* **74**, 2037–2044.

Motokawa T, Shintani O, & Birenheide R (2004) Contraction and stiffness changes in collagenous arm ligaments of the stalked crinoid *Metacrinus rotundus* (Echinodermata). *Biol Bull* **206**, 4–12.

Mulloney B & Selverston AI (1974a) Organization of the stomatogastric ganglion of the spiny lobster I: neurons driving the lateral teeth. *J Comp Physiol* **91**, 1–32.

Mulloney B & Selverston AI (1974b) Organization of the stomatogastric ganglion of the spiny lobster III: coordination of the two subsets of the gastric system. *J Comp Physiol* **91**, 53–78.

Owaki D & Ishiguro A (2017) A quadruped robot exhibiting spontaneous gait transitions from walking to trotting to galloping. *Sci Rep* **7**, 277.

Owaki D, Kano T, Nagasawa K, Tero A, & Ishiguro A (2013) Simple robot suggests physical interlimb communication is essential for quadruped walking. *J Royal Soc Interface* **10**, 20120669.

Paul CRC & Smith AB (1984) The early radiation and phylogeny of echinoderms. *Biol Rev* **59**, 443–481.

Pentreath RJ (1971) Respiratory surfaces and respiration in three New Zealand intertidal ophiuroids. *J Zool* **163**, 397–412.

Preyer WT (1887) *Die Bewegungen der Seesterne*. Berlin, Germany: Friedländer.

R Core Team (2018) R: a language and environment for statistical computing. https://www.R-project.org. Accessed 15 November 2018.

Romanes GJ & Ewart JC (1881) Observations on the locomotor system of Echinodermata. *Philos Trans Royal Soc* **172**, 829–885.

Schechter J & Lucero J (1968) A light and electron microscopic investigation of the digestive system of the ophiuroid *Ophiuroiderma panamensis* (brittle star). *J Morphol* **124**, 451–481.

Selverston AI & Mulloney B (1974) Organization of the stomatogastric ganglion of the spiny lobster II: neurons driving the medial teeth. *J Comp Physiol* **91**, 33–51.

Shen WM, Will P, Galstyan A, & Chuong CM (2004) Hormone-inspired self-organization and distributed control of robotic swarms. *Auton Robot* **17**, 93–105.

Smith JE (1937) II: on the nervous system of the starfish *Mathasterias glacialis* (L.). *Philos Trans Royal Soc B* **227**, 111–173.

Stan Development Team (2018) Stan modeling language users guide and reference manual, version 2.18.0. http://mc-stan.org. Accessed 15 November 2018.

Stein PS (1978) Motor systems, with specific reference to the control of locomotion. *Ann Rev Neurosci* **1**, 61–81.

Sumrall CD & Wray GA (2007) Ontogeny in the fossil record: diversification of body plans and the evolution of “aberrant” symmetry in Paleozoic echinoderms. *Paleobiology* **33**, 149–163.

Sutera SP & Skalak R (1993) The history of Poiseuille's law. *Ann Rev Fluid Mech* **25**, 1–20.

Suzuki R, Katsuno I, & Matano K (1971) Dynamics of “neuron ring”. *Kybernetik* **8**, 39–45.

Takamatsu A, Fujii T, & Endo I (2000) Time delay effect in a living coupled oscillator system with the plasmodium of *Physarum polycephalum*. *Phys Rev Lett* **85**, 2026–2029.

Takamatsu A, Tanaka R, Yamada H, Nakagaki T, Fujii T, & Endo I (2001) Spatiotemporal symmetry in rings of coupled biological oscillators of *Physarum* plasmodial slime mold. *Phys Rev Lett* **87**, 078102.

Takamatsu A, Tanaka R, & Fujii T (2004) Hidden symmetry in chains of biological coupled oscillators. *Phys Rev Lett* **92**, 228102.

Talpalar AE, Bouvier J, Borgius L, Fortin G, Pierani A, & Kiehn O (2013) Dual-mode operation of neuronal networks involved in left–right alternation. *Nature* **500**, 85.

Tejedo M, Semlitsch RD, & Hotz H (2000) Covariation of morphology and jumping performance in newly metamorphosed water frogs: effects of larval growth history. *Copeia* **2000**, 448–458.

Tsujita K, Tsuchiya K, & Onat A (2001) Adaptive gait pattern control of a quadruped locomotion robot. *Proc IEEE/RSJ Int Conf Intell Robot Syst* **4**, 2318–2325.

Uexküll JV (1905) Studien über den tonus II: die bewegungen der schlangensterne. *Z Biol* **46**, 1–37.

Umedachi T, Idei R, Ito K, & Ishiguro A (2013) A fluid-filled soft robot that exhibits spontaneous switching among versatile spatiotemporal oscillatory patterns inspired by the true slime mold. *Artif*

Life **19**, 67–78.

Umetani Y & Inou N (1985) Biomechanical study of peristalsis: neural mechanism of rhythmic segmentation. *J Soc Inst Contr Eng* **21**, 965–969.

Vásárhelyi G, Virágh C, Somorjai G, Tarcai N, Szörényi T, Nepusz T, & Vicsek T (2014) Outdoor flocking and formation flight with autonomous aerial robots. *Proc IEEE/RSJ Int Conf Intell Robot Syst* **27**, 3866–3873.

Vicsek T (2001) A question of scale. *Nature* **411**, 421.

Wadden T, Hellgren J, Lansner A, & Grillner S (1997) Intersegmental coordination in the lamprey: simulations using a network model without segmental boundaries. *Biol Cybern* **76**, 1–9.

Warner GF (1971) On the ecology of a dense bed of the brittle-star *Ophiothrix fragilis*. *J Mar Biol Assoc UK* **51**, 267–282.

Watanabe S (2009) *Algebraic Geometry and Statistical Learning Theory*. Cambridge, UK: Cambridge University Press.

Watanabe S (2010) Asymptotic equivalence of Bayes cross validation and widely applicable information criterion in singular learning theory. *J Mach Learn Res* **11**, 3571–3594.

Watanabe S (2018) *Mathematical Theory of Bayesian Statistics*. Florida, USA: CRC Press.

Watanabe W, Kano T, Suzuki S, & Ishiguro A (2011) A decentralized control scheme for orchestrating versatile arm movements in ophiuroid omnidirectional locomotion. *J Royal Soc Interface* **9**, 102–109.

Wilkie IC (1978) Functional morphology of the autotomy plane of the brittlestar *Ophiocomina nigra* (Abildgaard) (Ophiuroidea, Echinodermata). *Zoomorphologie* **91**, 289–305.

Yasui K, Sakai K, Kano T, Owaki D, & Ishiguro A (2017) Decentralized control scheme for myriapod robot inspired by adaptive and resilient centipede locomotion. *PLoS ONE* **12**, e0171421.

Yee A, Burkhardt J, & Gilly WF (1987) Mobilization of a coordinated escape response by giant axons in the ophiuroid, *Ophiopteris papillosa*. *J Exp Biol* **128**, 287–305.

Zueva O, Khoury M, Heinzeller T, Mashanova D, & Mashanov V (2018) The complex simplicity of the brittle star nervous system. *Front Zool* **15**, 1.

TABLE

Table 1. WAICs of statistical models for Θ, B_α, and $E_{\alpha\beta}$ in "2. Locomotion of *Ophiactis brachyaspis*."

Model	Specification		Four-armed			Five-armed			Six-armed			Seven-armed		
			Rank	WAIC	Δ	Rank	WAIC	Δ	Rank	WAIC	Δ	Rank	WAIC	Δ
Θ	Distribution number													
1	one		2	0.876	0.917	2	1.192	0.764	2	1.518	5.55	2	1.860	10.7
2	two		1	0.845	**0***	1	1.179	**0***	1	1.425	**0***	1	1.502	**0***
B_α	Explanatory variable†	Individuality†												
1	no	no	3	4.217	4.94	8	4.671	60.4	5	5.338	58.9	4	4.940	25.7
2	no	yes	—	—	—	9	4.676	61.9	10	5.352	64.0	—	—	—
3	L_α	no	1	4.176	**0***	10	4.679	62.9	9	5.350	63.2	5	4.956	29.0
4	L_α	yes	—	—	—	12	4.688	65.4	12	5.382	74.9	—	—	—
5	S	no	5	4.267	10.9	7	4.670	60.3	7	5.338	59.2	3	4.879	12.8
6	S	yes	—	—	—	11	4.680	63.1	11	5.360	67.0	—	—	—
7	Θ	no	2	4.187	1.29	1	4.469	**0***	2	5.191	6.25	2	4.827	2.03
8	Θ	yes	—	—	—	2	4.477	2.16	4	5.208	12.2	—	—	—
9	Θ_{sign}	no	4	4.230	6.41	3	4.501	9.43	1	5.174	**0***	1	4.818	**0***
10	Θ_{sign}	yes	—	—	—	4	4.505	10.8	3	5.193	6.89	—	—	—
11	F_α	no	6	4.271	11.3	5	4.640	51.0	6	5.338	59.1	6	4.955	28.8
12	F_α	yes	—	—	—	6	4.644	52.3	8	5.347	62.4	—	—	—
$E_{\alpha\beta}$	Explanatory variable†													
1	no		1	3.951	**0***	4	4.327	25.6	4	4.440	42.0	3	4.294	9.30
2	S		4	3.974	4.14	3	4.321	22.0	2	4.413	17.5	4	4.308	18.0
3	Θ		2	3.953	0.365	2	4.292	4.90	3	4.416	20.0	2	4.282	1.58
4	Θ_{sign}		3	3.959	1.45	1	4.284	**0***	1	4.394	**0***	1	4.279	**0***

*$\Delta = 0$ (bolded) indicates a best supportive model. †"No" indicates the explanatory variable or individuality was not considered; otherwise, it was considered in the mean of normal distribution.

FIGURES

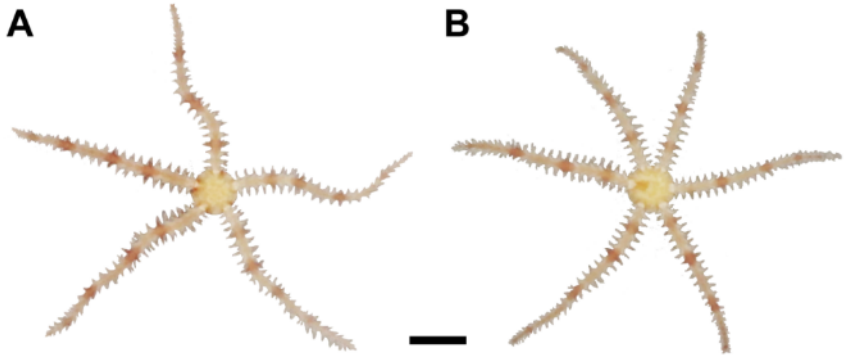

Fig. 1. The fissiparous brittle star *Ophiactis brachyaspis*. A: five-armed individual. **B:** six-armed individual. The scale bar represents 2 mm.

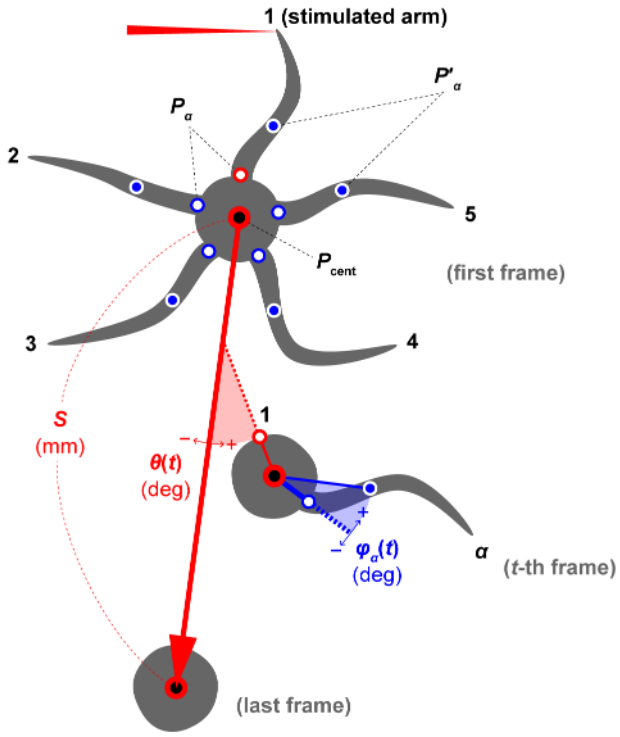

Fig. 2. Measurements of the locomotion of a brittle star (*Ophiactis brachyaspis*). Schematic five-armed brittle stars are shown at the first (t = 1), t-th, and last (t = 600) frames as an example. Not all arms are shown except for the first frame. The arm index, α, takes the values of 1 to 5, in which the stimulated arm is numbered 1. Blue-filled circles indicate the coordinate points of $P'_\alpha(t)$, while open circles show those of $P_\alpha(t)$. $P_1(t)$ is indicated by red-lined open circles. The center of gravity of $P_\alpha(t)$, namely $P_{cent}(t)$, is represented by red-lined filled circles. $\varphi_\alpha(t)$ is the arm angle formed by $P_\alpha(t)$, $P_{cent}(t)$, and $P'_\alpha(t)$. $\theta(t)$ is the angle formed by the segment $P_{cent}(1)P_{cent}(600)$ and $P_1(t)P_{cent}(t)$, representing the direction of the stimulated arm compared to the moving direction. The moving distance S corresponds to the length of the segment $P_{cent}(1)P_{cent}(600)$.

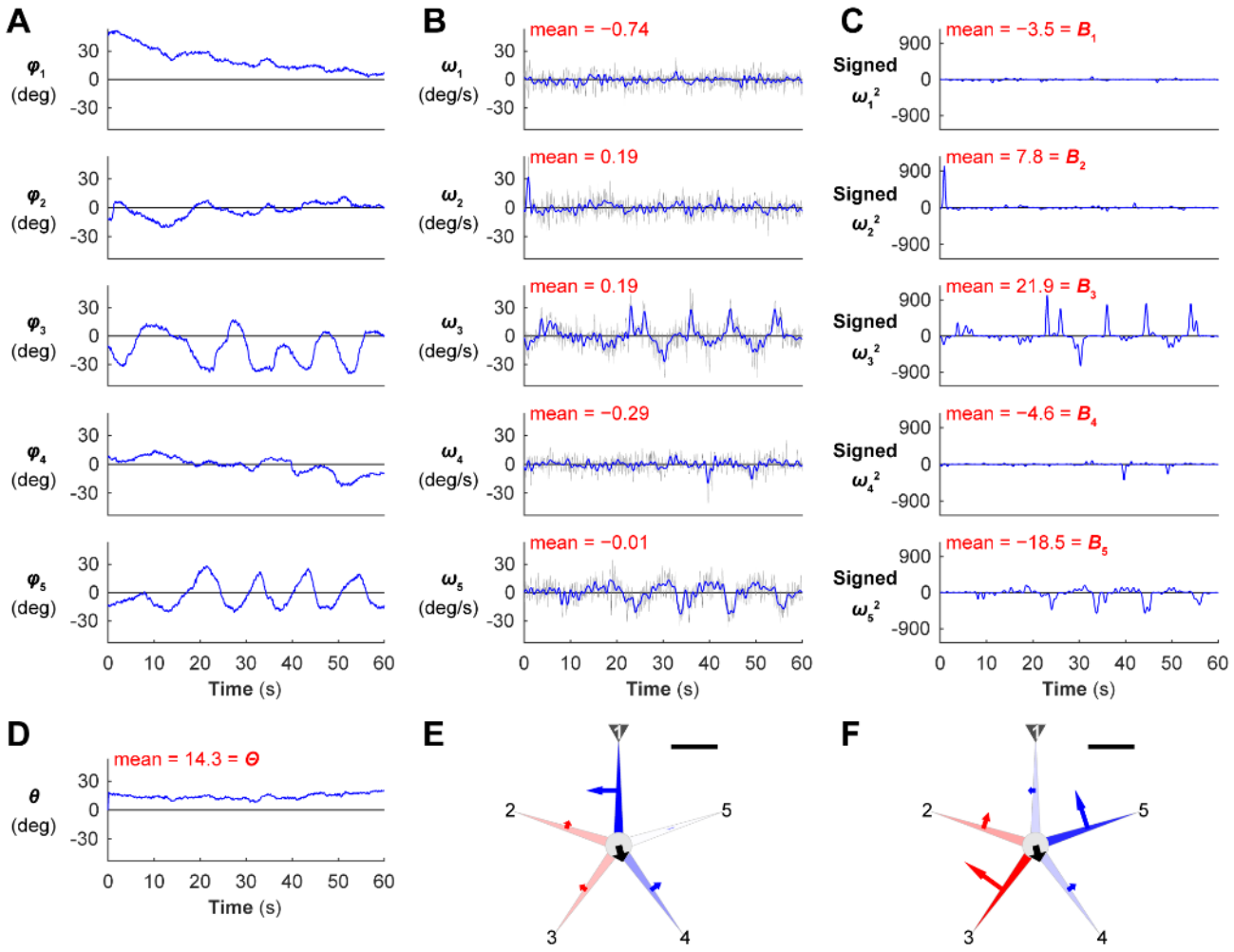

Fig. 3. Calculation and visualization of the locomotion of a five-armed brittle star (*Ophiactis brachyaspis*). A: temporal change of $\varphi_\alpha(t)$ (deg) (c.f. Fig. 2). **B:** temporal change of $\omega_\alpha(t)$ (deg/s)—angular velocity of $\varphi_\alpha(t)$. Background grey plots represent the original data, while thicker blue plots show low-pass filtered data. Each plot's "mean" indicates the mean value of the filtered $\omega_\alpha(t)$ for t = 1, 2, ..., 600. **C:** temporal change of signed $\omega_\alpha(t)^2$. Each plots' "mean" indicates its mean value for t = 1, 2, ..., 600, corresponding to B_α—the tendency of being a left or right rower in the α-th arm (Equation 3). **D:** temporal change of $\theta(t)$ (deg) (c.f. Fig. 2). "Mean" indicates its mean value for t = 1, 2, ..., 600, corresponding to Θ (deg)—moving direction (Equation 1). **E:** schematized brittle star reflecting the mean $\omega_\alpha(t)$ calculated in B and Θ in D. **F:** schematized brittle star reflecting B_α in C and Θ in D. In E and F, each grey arrowhead indicates the stimulated arm numbered 1, with the numbers following in order anticlockwise. The angles of black arrows at the disks represent Θ. Arms with negative/positive mean values extend blue-leftward/red-rightward arrows, respectively, with the arrows' length corresponding to the absolute value of its mean. Compared to the mean values of the original $\omega_\alpha(t)$ in E, B_α in F well explains actual locomotion. Note that B_α originally reflects a returning direction based on its sign (positive B_α denotes anticlockwise returning), but its schematized arrow indicates a 'pushing direction' for simply imagining force to the ground (positive B_α denotes clockwise pushing, thus apparently opposing the sign in Fig. 2). Scale bars represent 1.0 for the mean $\omega_\alpha(t)$ in E and 20 for B_α in F.

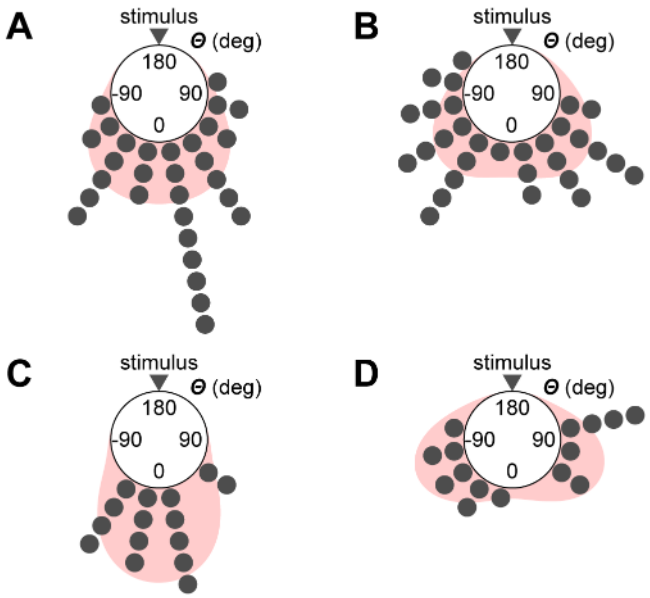

Fig. 4. Circular plots of moving direction after aversive tactile stimulation in brittle stars (*Ophiactis brachyaspis*). A: five-armed case (10 individuals, 30 trials). **B:** six-armed case (10 individuals, 30 trials). **C:** four-armed case (one individual, 15 trials). **D:** seven-armed case (one individual, 15 trials). The moving direction Θ is the measured angle based on the position of a mechanically stimulated arm (c.f. Figs 2, 3, Equation 1). Θ is 0 deg when the disk moves in the opposite direction to the stimulated arm, and is negative/positive when the disk movement is angled clockwise/anticlockwise, respectively, from the 0 deg. Each point represents Θ in each trial, which is grouped in a bin divided per 22.5 deg. Density plots on the background represent predictive distributions on the assumption of two symmetric von Mises distributions.

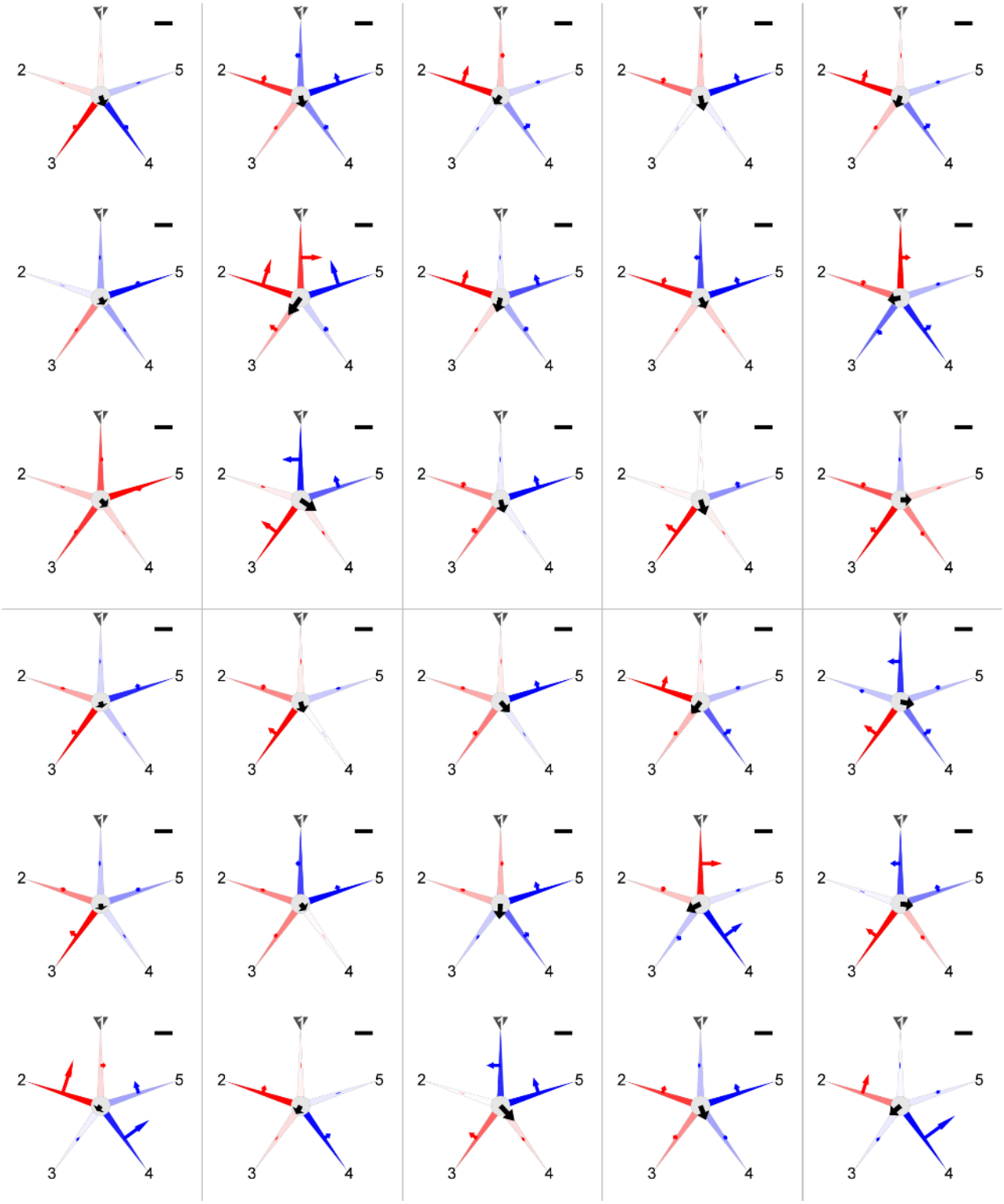

Fig. 5. Trial-by-trial locomotion of five-armed brittle stars (*Ophiactis brachyaspis*). Three trials per individual were analyzed in 10 individuals, which are partitioned by gray lines. Black arrows at the disks represent moving distance (S; c.f. Fig. 2) by length and moving direction (Θ; c.f. Figs 2, 3) by angle. Arms with negative/positive values for the tendency of being left or right rowers (B_α; c.f. Figs 2, 3) extend blue-leftward/red-rightward arrows, respectively, with the arrows' length corresponding to $|B_\alpha|$. In each panel, the arm with the maximum $|B_\alpha|$ is colored with the darkest blue/red, while the other arms show lighter blue/red corresponding to the relative values to the maximum. Scale bars represent 20 mm for S and 50 for B_α.

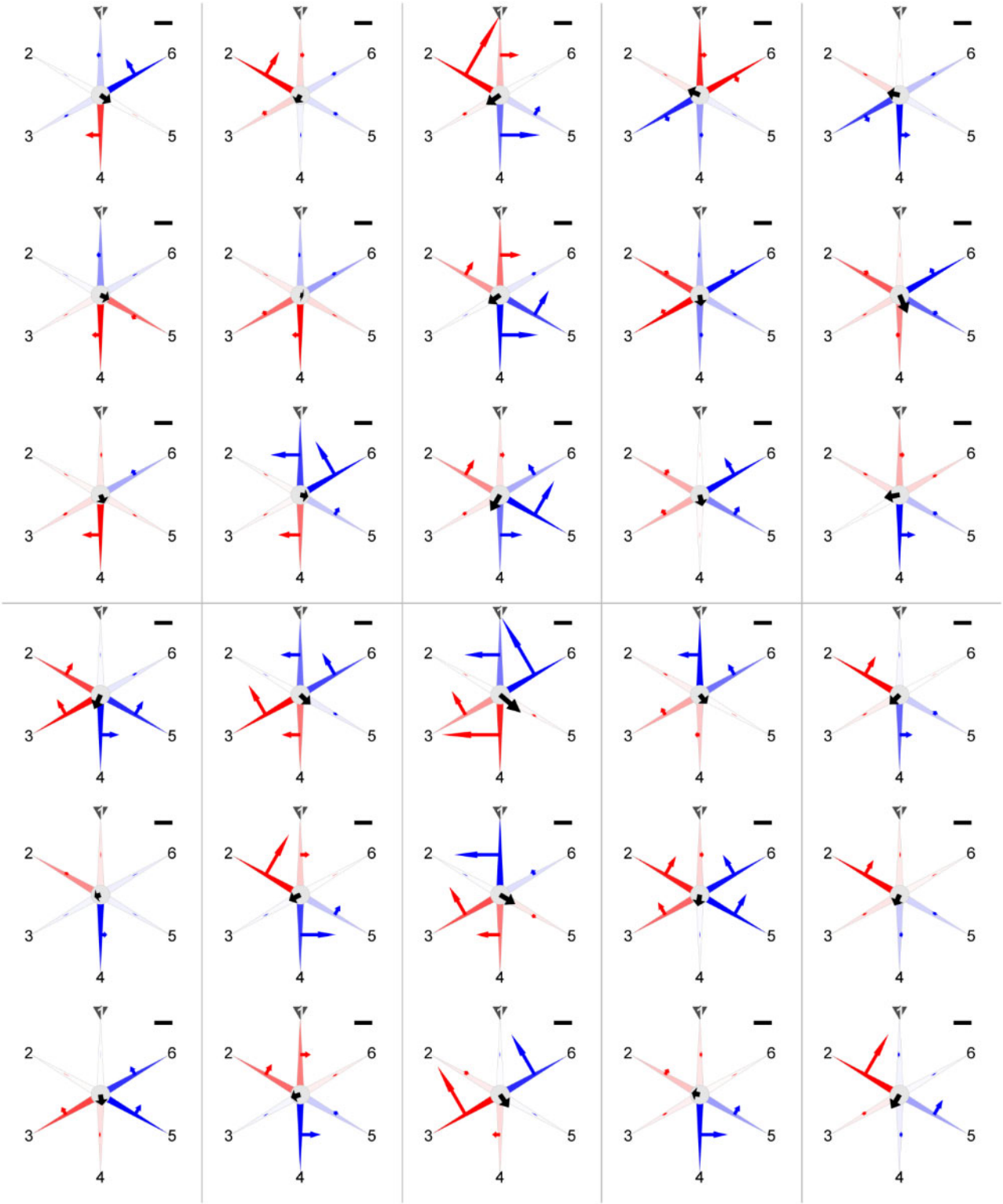

Fig. 6. Trial-by-trial locomotion of six-armed brittle stars (*Ophiactis brachyaspis*). Three trials per individual were analyzed in 10 individuals, which are partitioned by gray lines. Results are shown as in Fig. 5.

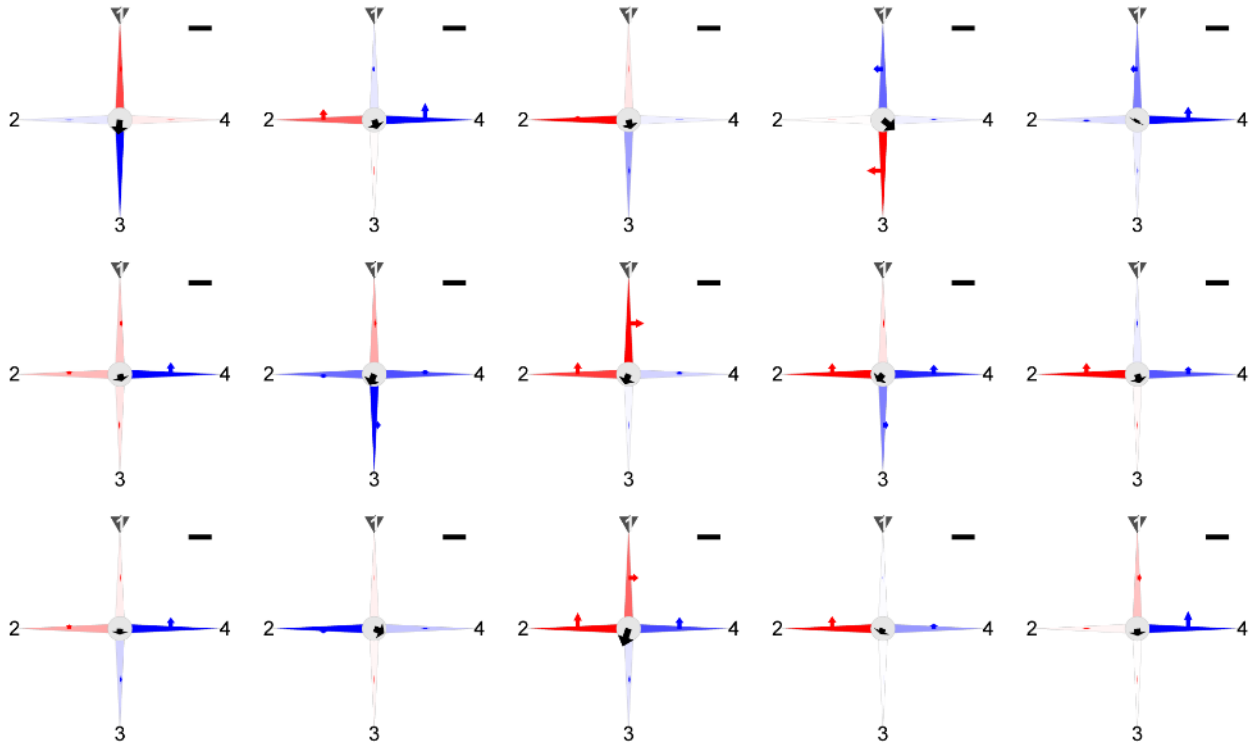

Fig. 7. Trial-by-trial locomotion of a four-armed brittle star (*Ophiactis brachyaspis*). Fifteen trials were analyzed in one individual. Results are shown as in Fig. 5.

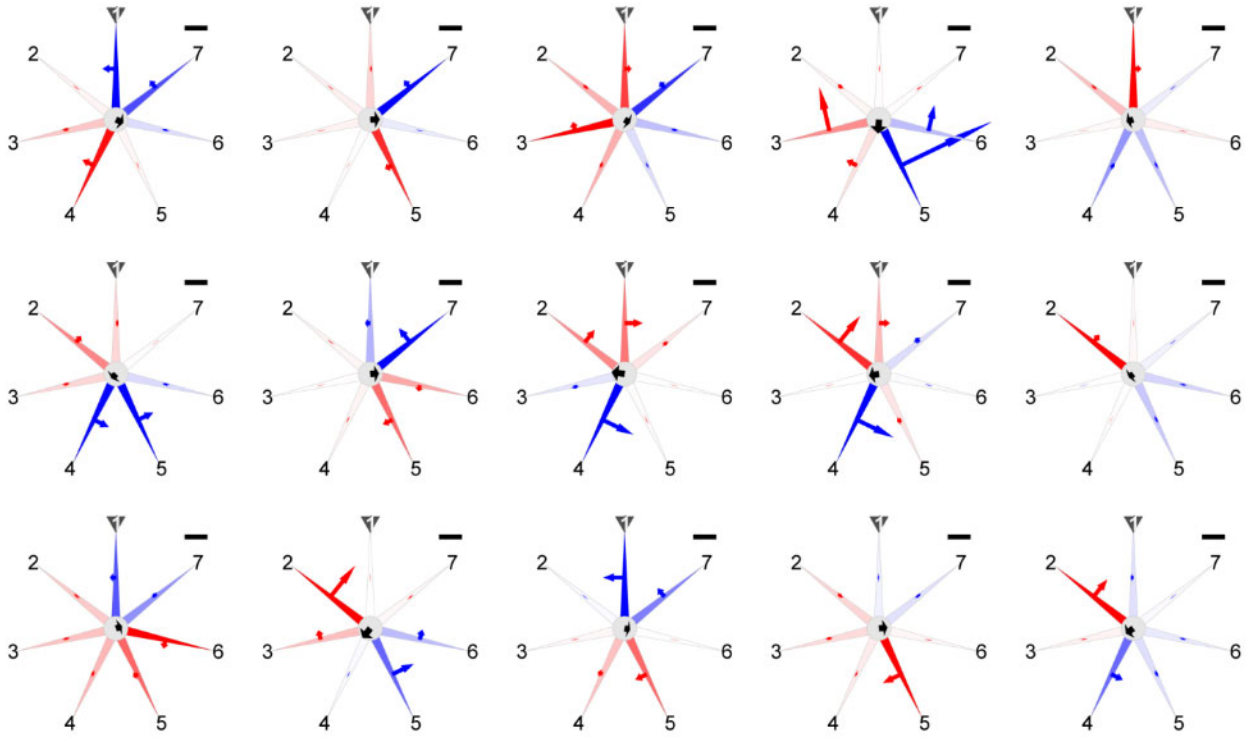

Fig. 8. Trial-by-trial locomotion of a seven-armed brittle star (*Ophiactis brachyaspis*). Fifteen trials were analyzed in one individual. Results are shown as in Fig. 5.

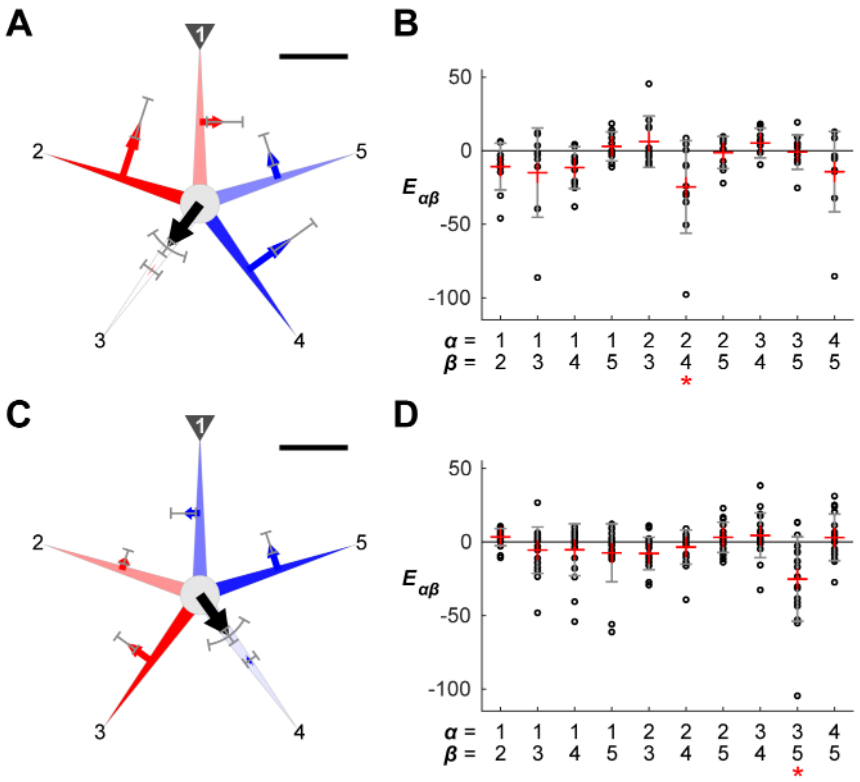

Fig. 9. Locomotion of five-armed brittle stars (*Ophiactis brachyaspis*) grouped by moving direction. A, B: case in which moving direction (Θ; c.f. Figs 2, 3, Equation 1) is angled clockwise from the opposite direction to the stimulated arm, i.e., Θ is negative and Θ_{sign} = 0 (eight individuals, 11 trials). **C, D:** case in which Θ is positive (angled clockwise), i.e., Θ_{sign} = 1 (10 individuals, 19 trials). **A, C:** schematized brittle stars reflecting the resultant quantitative values. Black arrows at the disks represent the measured means of moving distance (S; c.f. Fig. 2) by length and the measured means of Θ by angle. Error bars parallel to the disks' arrows show S's standard deviation (s.d.), and arc-shaped error bars represent Θ's s.d. in data. The blue or red arrow at each arm represents the tendency of being a left or right rower (B_α; c.f. Figs 2, 3, Equation 3), reflecting the absolute median of each posterior mean by arrow length and the median of each posterior s.d. by error bars. When a posterior mean was negative/positive, its blue-leftward/red-rightward arrow extends from its arm, indicating that the arm pushed leftward/rightward (anticlockwise/clockwise), respectively. In each panel, the arm with the maximum absolute value in posterior mean is colored with the darkest blue/red, while the other arms show lighter blue/red corresponding to the relative values to the maximum. Scale bars represent 40 mm for S and 50 for B_α. **B, D:** degree of synchronization between two arms ($E_{\alpha\beta}$ for the α- and β-th arms; Equation 4). Small circles represent measured data. Pair-by-pair red pluses indicate the medians of posterior means, while error bars show the medians of posterior s.d. parameters. Negative/positive values represent that the paired movement of the α- and β-th arms synchronized in the opposite/same direction, respectively. Each asterisk indicates the pair with the largest negative estimated mean, showing remarkable antiphase synchronization. These pairs correspond to those with strong average leftward/rightward biases in A and C. All posterior distributions for both B_α and $E_{\alpha\beta}$ were estimated under a best performed model in terms of WAIC, in which Θ_{sign} is an explanatory variable for the mean and s.d.

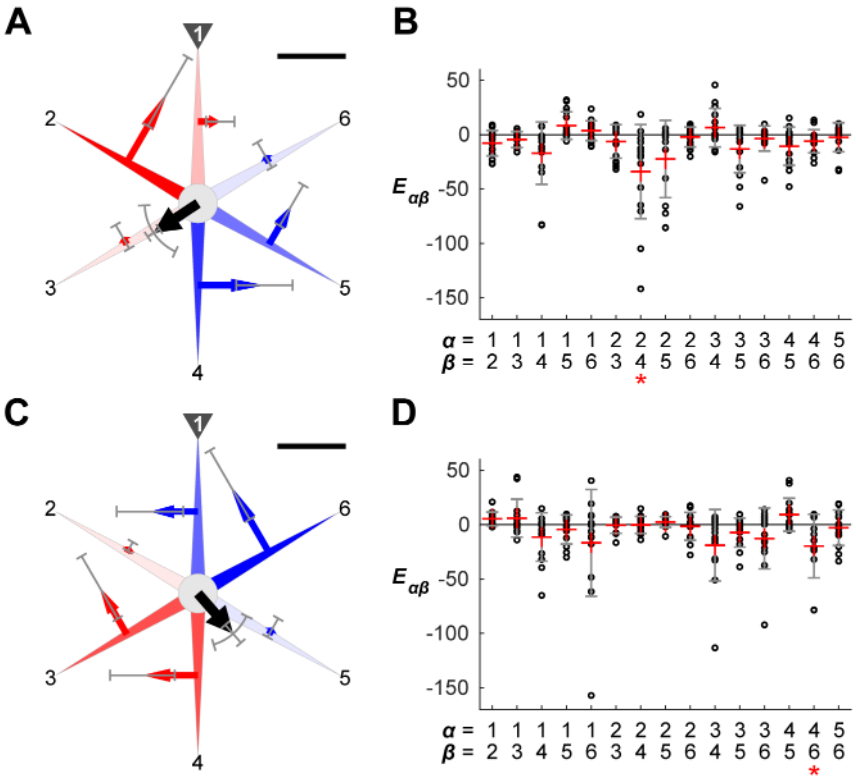

Fig. 10. Locomotion of six-armed brittle stars (*Ophiactis brachyaspis*) grouped by moving direction. A, B: case in which Θ_{sign} = 0 (eight individuals, 16 trials). **C, D:** case in which Θ_{sign} = 1 (eight individuals, 14 trials). **A, C:** schematized brittle stars reflecting the resultant quantitative values, as explained in Fig. 9. **B, D:** degree of synchronization between two arms ($E_{\alpha\beta}$ for the α- and β-th arms; Equation 4), as explained in Fig. 9.

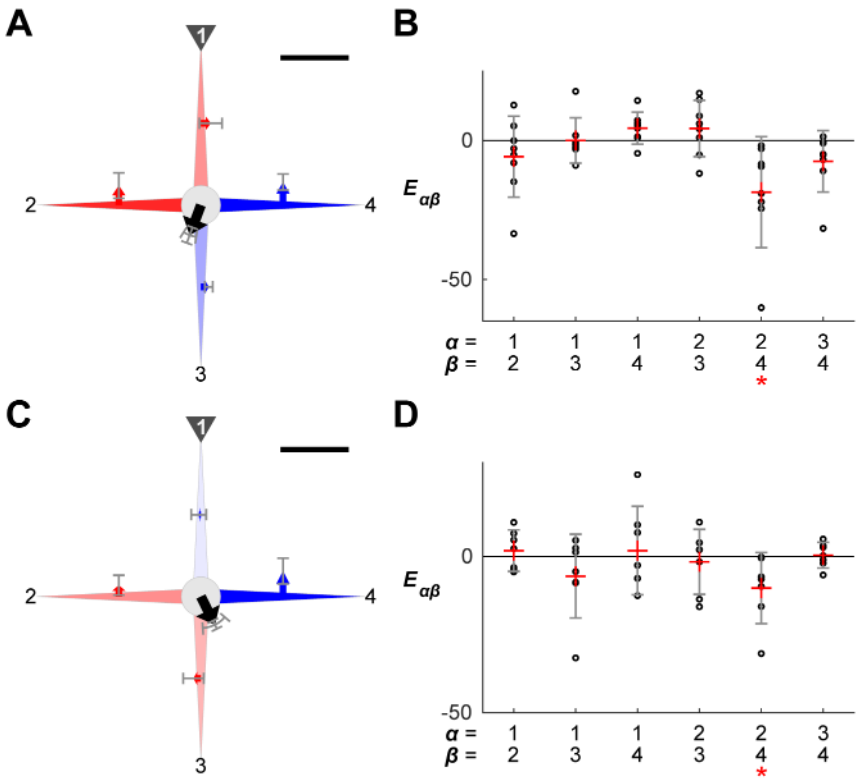

Fig. 11. Locomotion of a four-armed brittle star (*Ophiactis brachyaspis*) grouped by moving direction. A, B: case in which Θ_{sign} = 0 (one individual, eight trials). **C, D:** case in which Θ_{sign} = 1 (one individual, seven trials). **A, C:** schematized brittle stars reflecting the resultant quantitative values, as explained in Fig. 9. **B, D:** degree of synchronization between two arms ($E_{\alpha\beta}$ for the α- and β-th arms; Equation 4), as explained in Fig. 9.

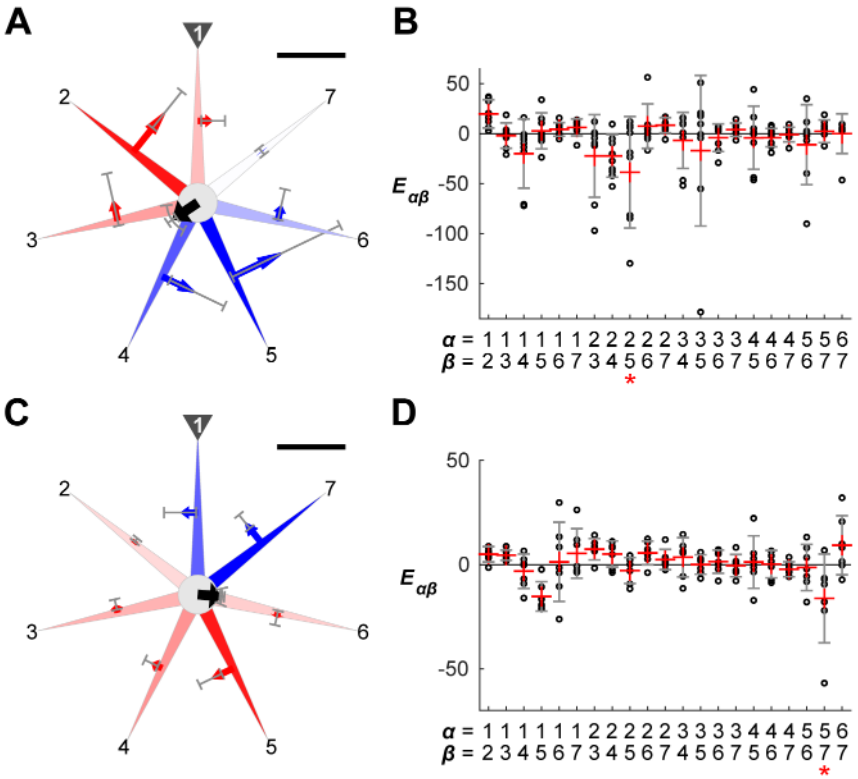

Fig. 12. Locomotion of a seven-armed brittle star (*Ophiactis brachyaspis*) grouped by moving direction. **A, B:** case in which Θ_{sign} = 0 (one individual, eight trials). **C, D:** case in which Θ_{sign} = 1 (one individual, seven trials). **A, C:** schematized brittle stars reflecting the resultant quantitative values, as explained in Fig. 9. **B, D:** degree of synchronization between two arms ($E_{\alpha\beta}$ for the α- and β-th arms; Equation 4), as explained in Fig. 9.

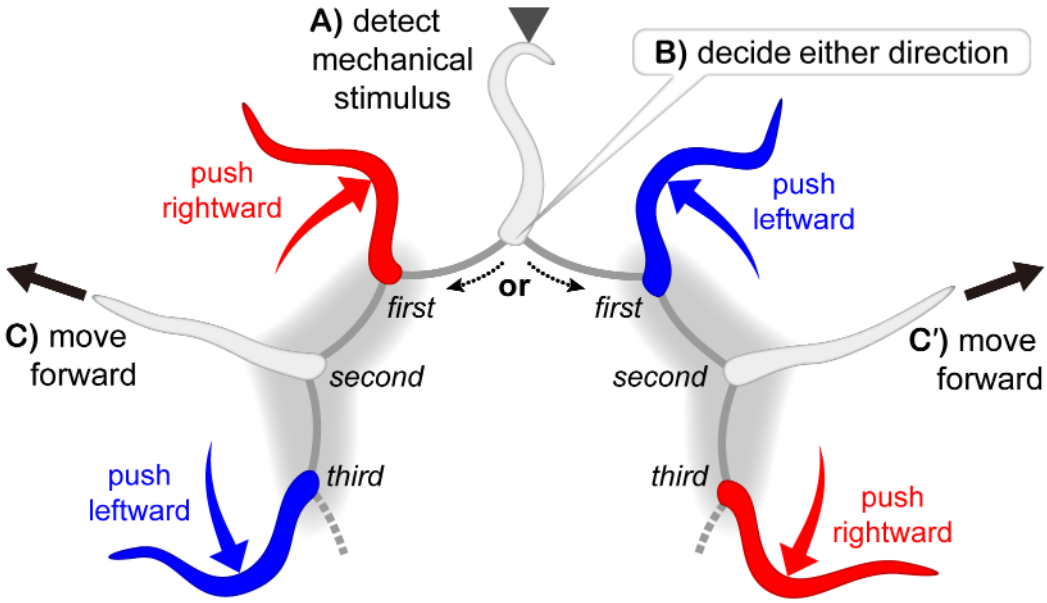

Fig. 13. Model of arm-by-arm locomotive movements in brittle stars with a variable number of arms after aversive tactile stimulation. The stimulated arm makes an afferent signal—**(A)**—which chiefly transfers through inter-arm connections (clockwise or anticlockwise), represented by the circumoral nerve ring. The direction in which the signal dominates is determined by some perturbation—**(B)**. Subsequently, one of the *first* neighboring arms to the stimulated arm actively pushes the ground in the stimulus direction, while the *third* neighbor (in the same direction) synchronously pushes in the opposite direction to the *first*. As a result, the *second* arm between the *first* and *third* faces forward in behavioral terms—**(C)** or **(C')**.

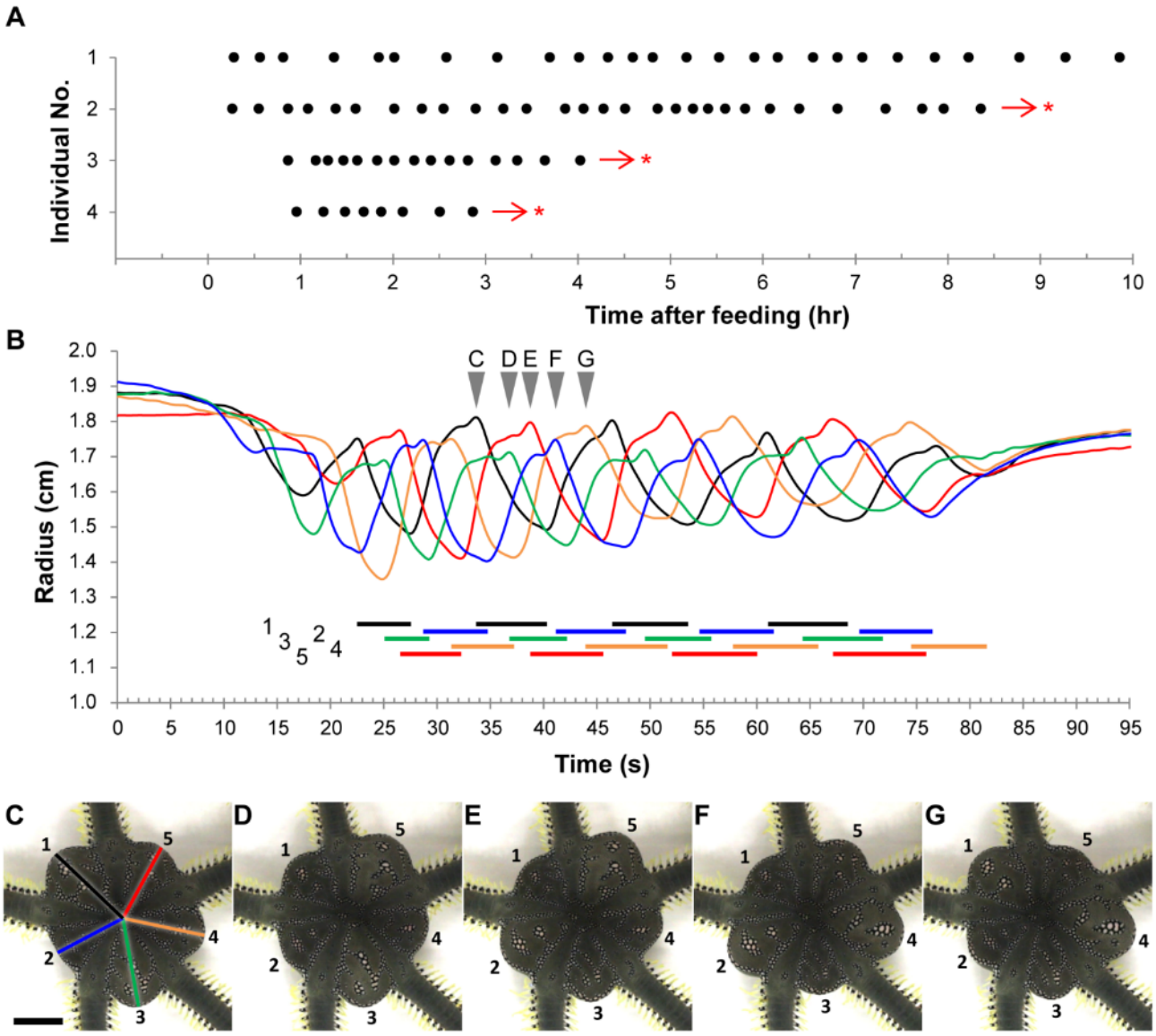

Fig. 14. Rhythmic movement, "pumping," in the five-armed individuals of the green brittle star (*Ophiarachna incrassata*). A: temporal frequency of pumping phases. Each point represents a pumping phase, which comprises a series of movements shown in B. The animals exhibited the first pumping phase 36 ± 17 min (four individuals) after feeding. Then, they periodically showed pumping for more than 10 hrs. The interval between pumping phases was not consistent (20 ± 9 min) among individuals. Asterisks indicate no record from the arrows. **B:** temporal change in the radius of the five interradii in a pumping phase. Radius was measured from the center of the disk to the midpoint of the edge of each interradius. The radii numbered anticlockwise are colored as in C, which corresponds to B in color. Colored horizontal bars under the graph represent shrinking periods of each interradius. **C–G:** aboral view of the individual at the moments indicated by the arrowheads in B. The scale bar represents 10 mm.

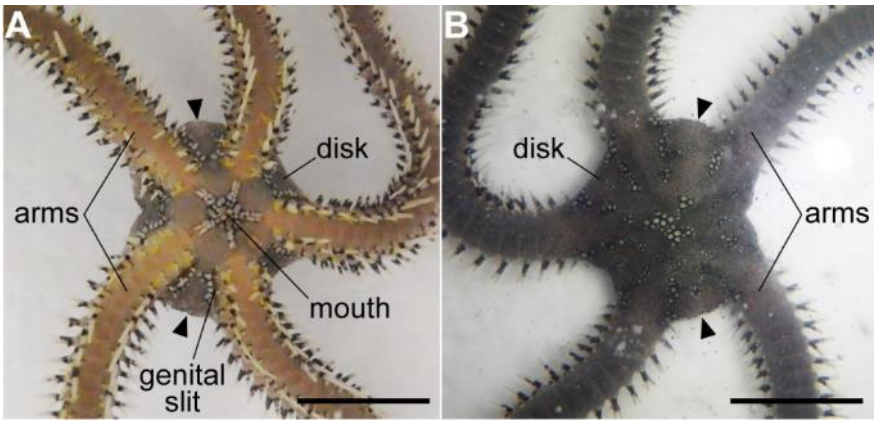

Fig. 15. Frozen individual at the moment of rhythmic movement, "pumping," in the green brittle star (*Ophiarachna incrassata*). A: oral view. **B:** aboral view. Photos were taken just after pouring −80°C ethanol while pumping was observed at the disk. Arrowheads denote well-expanding portions. Scale bars represent 10 mm. Scanned and segmented images of this specimen are shown in Fig. 17.

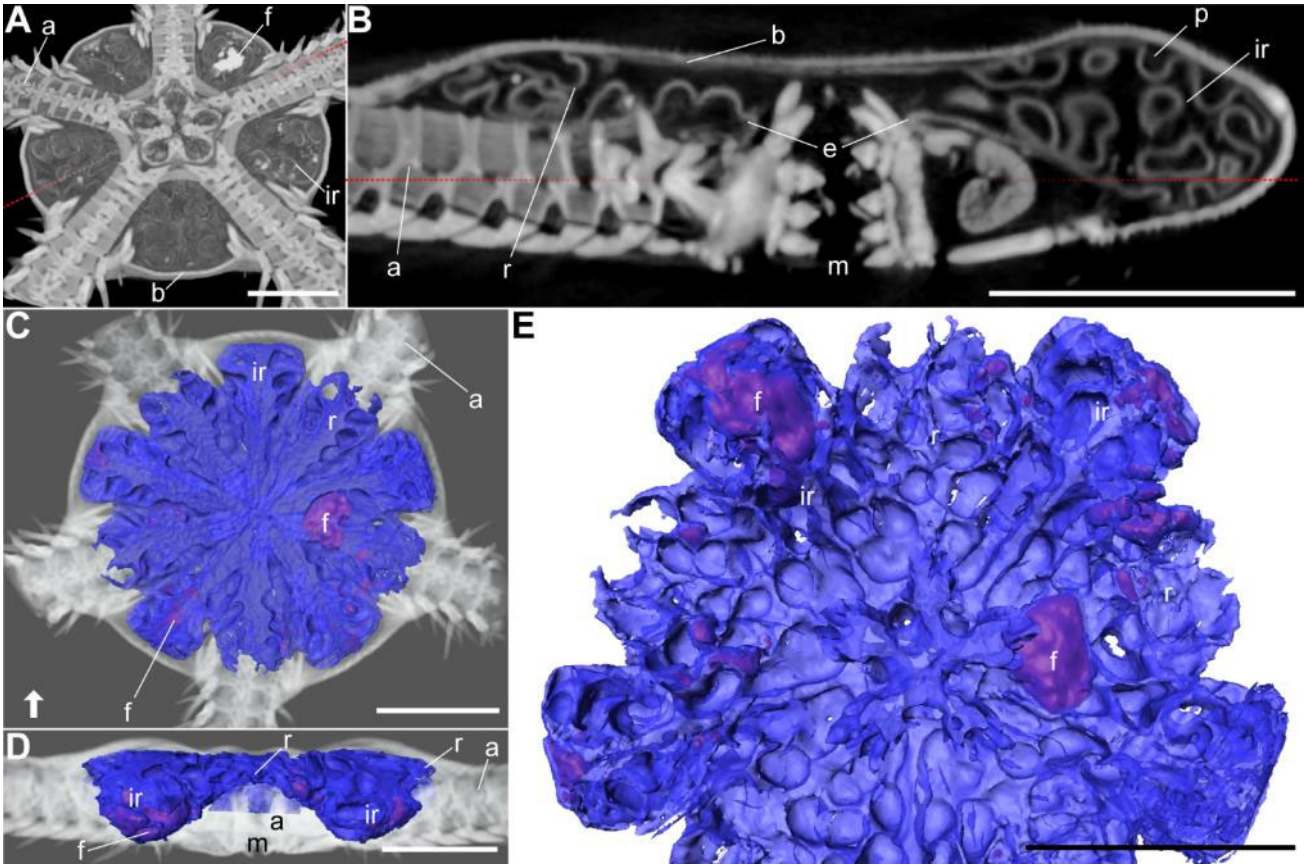

Fig. 16. Internal structure of the disk of a five-armed relaxed individual in the green brittle star (*Ophiarachna incrassata*). Body structure was scanned with X-ray micro-computed tomography (micro-CT) and reconstructed in three dimensions, which is displayed in grayscale. The internal lining of the digestive tract beginning from the mouth is colored blue. Contents in the stomach are colored red. **A:** reconstructed images viewed from the oral side, sectioned at a plane shown in B by the red dotted line. **B:** oral-aboral section on a plane indicated in A by the red dotted line; the bottom is oral; slice thickness is 0.38 μm. **C:** aboral view of the segmented model. **D:** lateral view of the segmented model from the side indicated in C by the arrow; the bottom is oral; the front side of the grayscale images is truncated. **E:** enlarged oral view of the segmented model. Abbreviations: a, arm skeleton; b, body wall; e, esophagus; f, food (gut content); ir, interradial pouch; m, mouth; p, perivisceral coelom; r, radial pouch. Scale bars represent 5 mm.

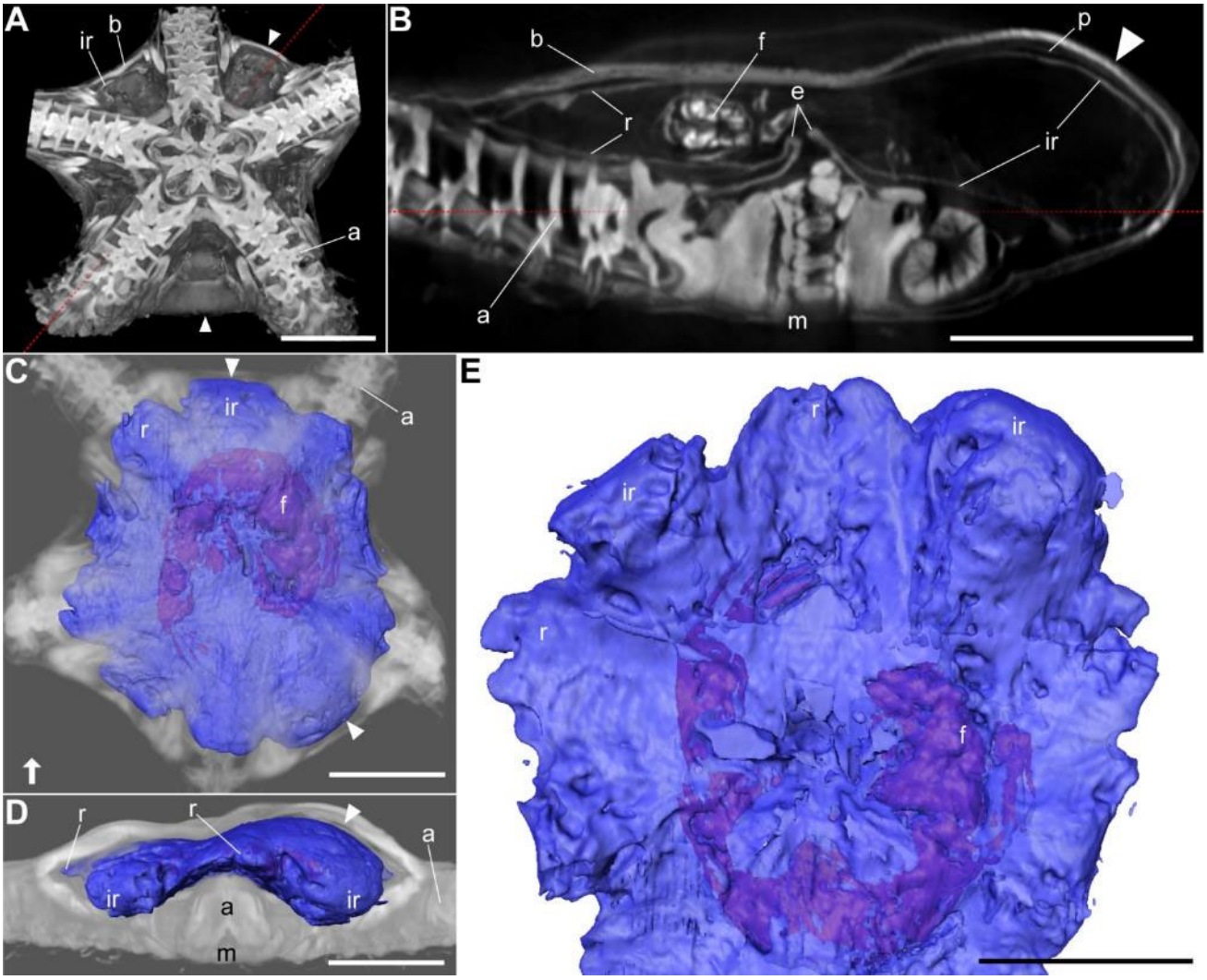

Fig. 17. Internal structure of the disk of a five-armed individual during rhythmic movement, "pumping," in the green brittle star (*Ophiarachna incrassata*). Body structure of an instantly frozen individual shown in Fig. 15 was scanned with X-ray micro-computed tomography (micro-CT) and reconstructed in three dimensions, which is displayed in grayscale. The internal lining of the digestive tract beginning from the mouth is colored blue. Contents in the stomach are colored red. Arrowheads denote well-expanding portions. **A:** reconstructed images viewed from the oral side, sectioned at a plane shown in B by the red dotted line. **B:** oral-aboral section on a plane indicated in A by the red dotted line; the bottom is oral; slice thickness is 0.36 μm. **C:** aboral view of the segmented model. **D:** lateral view of the segmented model from the side indicated in C by the arrow; the bottom is oral; the front side of the grayscale images is truncated. **E:** enlarged oral view of the segmented model. Abbreviations: a, arm skeleton; b, body wall; e, esophagus; f, food (gut content); ir, interradial pouch; m, mouth; p, perivisceral coelom; r, radial pouch. Scale bars represent 5 mm.

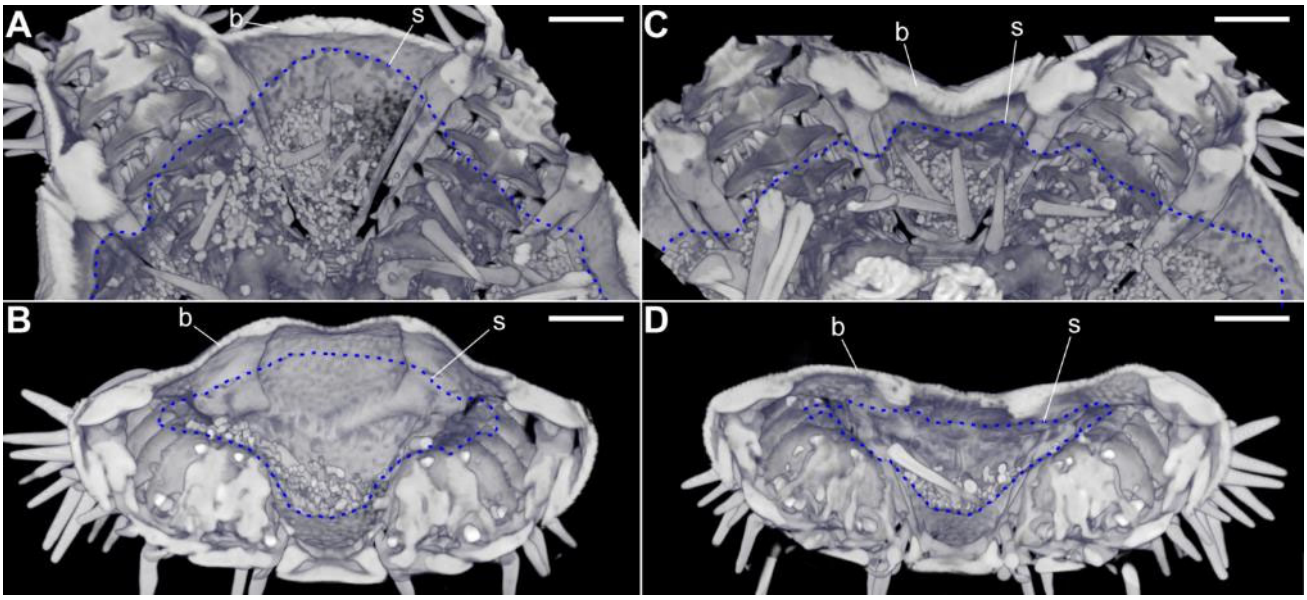

Fig. 18. Internal structure of expanding and shrinking interradii in a five-armed individual during rhythmic movement, "pumping," in the green brittle star (*Ophiarachna incrassata*). Body structure of an instantly frozen individual (different from that in Figs 15 and 17) was scanned with X-ray micro-computed tomography (micro-CT) and reconstructed in three dimensions, which is displayed in grayscale. The internal lining of the stomach is denoted by blue dotted lines. **A:** aboral view of an expanding interradius, sectioned at a horizontal plane. **B:** lateral view of an expanding interradius, sectioned at a vertical plane. **C:** aboral view of a shrinking interradius, sectioned at a horizontal plane. **D:** lateral view of a shrinking interradius, sectioned at a vertical plane. The bottom is the disk's center in A and C and the oral side in B and D. Abbreviations: b, body wall; s, stomach wall. Scale bars represent 2 mm.

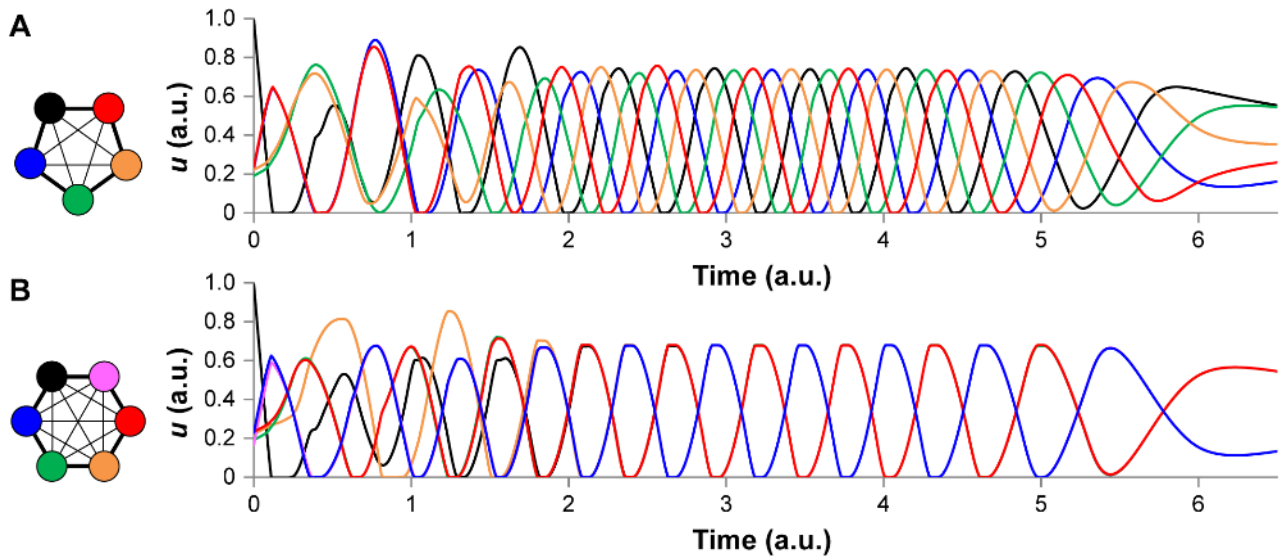

Fig. 19. Simulation of rhythmic movement, "pumping," in the green brittle star (*Ophiarachna incrassata*) based on a phenomenological model. A: temporal change of the volume of five interradii. Cycles are unsynchronized as in the experiments of five-armed individuals (Fig. 14B). **B:** temporal change of the volume of six interradii. Three distant interradii and the other three each make synchronized groups, anticipating the coordinated pattern of six-armed individuals. In y-axes, *u* represents the volume of internal fluid in each interradius. Each axis is given in an arbitrary unit. The color of the interradii in each inset corresponds to that of each graph. The black one in each panel represents the first interradius, which initially has a larger volume than the others.

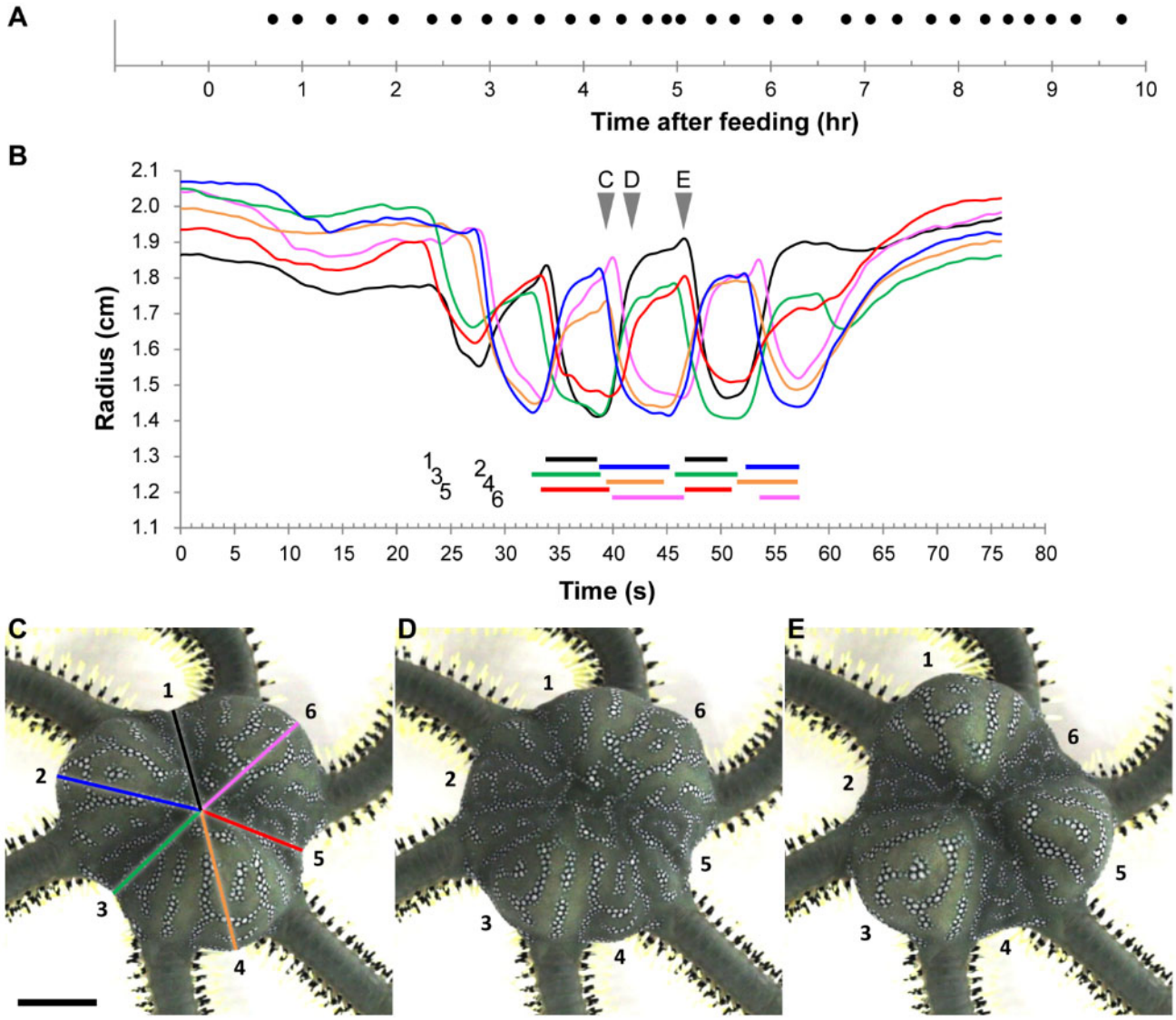

Fig. 20. Rhythmic movement, "pumping," in the six-armed individual of the green brittle star (*Ophiarachna incrassata*). A: temporal frequency of pumping phases. The animal frequently showed pumping phases for more than 10 hrs after feeding, as occurs in five-armed animals (Fig. 14A). **B:** temporal change in the radius of the six interradii in a pumping phase. Cycles synchronized with a separation of two groups, which demonstrates the model simulation of six interradii (Fig. 19B). **C–E:** aboral view of the individual at the moments indicated by the arrowheads in B. The scale bar represents 10 mm. Figures are shown as in Fig. 14.

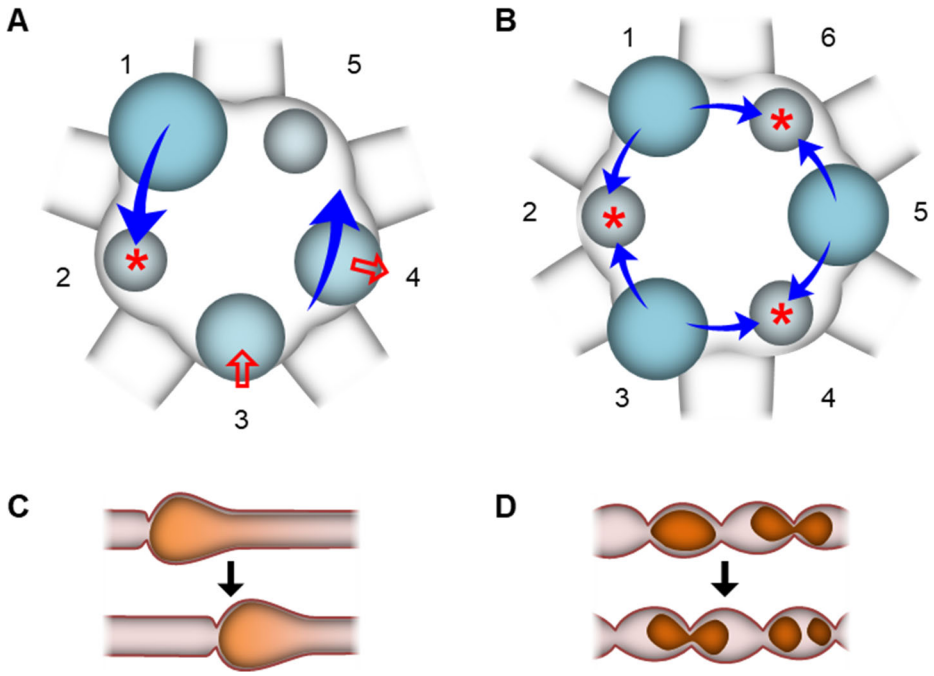

Fig. 21. Possible fluid flows in the disk during rhythmic movement, "pumping," and its function in brittle stars. Circles represent fluid-filled interradial spaces inside the stomach, which shrink/expand during pumping. Blue filled arrows represent fluid flows between interradii. Red asterisks indicate interradii that start expansion next. **A:** scheme of pumping in a five-armed disk making a traveling wave; red open arrows indicate interradii that are shrinking or expanding at the moment. **B:** scheme of pumping in a six-armed disk making a stationary wave. **C:** scheme of intestinal peristalsis to carry liquid contents, for comparison with A. **D:** scheme of intestinal segmentation to mix solid contents, for comparison with B.

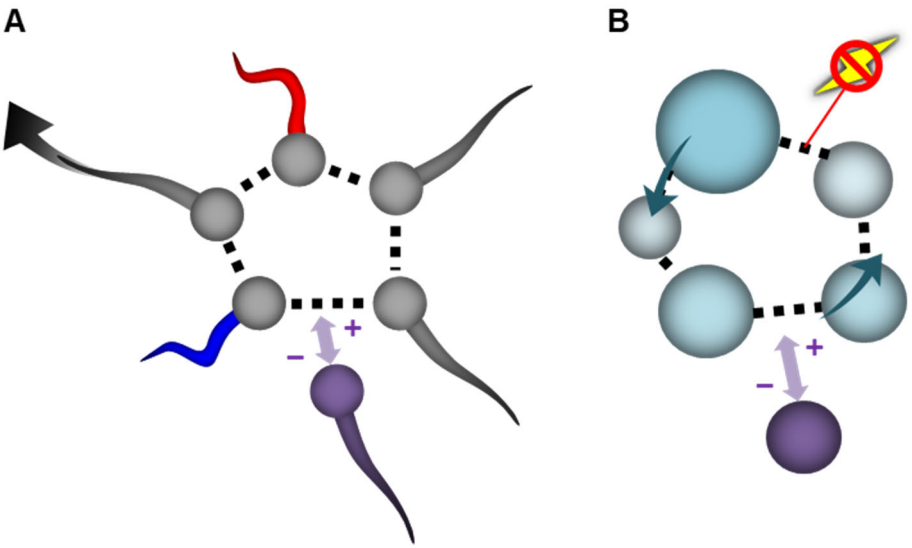

Fig. 22. Robotics application of number-flexible coordinating networks that can exist in brittle stars. **A:** design of a locomotive robot inspired by a possible neural network coordinating the post-stimulus locomotion of brittle stars (c.f. Fig. 13). Addition or subtraction of armed units can change the trajectory of the robot in response to external stimulation (c.f. Fig. 4). **B:** design of a circulating/mixing robot inspired by a possible non-neural network coordinating a pumping movement in brittle stars (c.f. Fig. 21). Addition or subtraction of contractile units can change the way of internal flows.

ACHIEVEMENTS

Journal articles

Wakita D, Hayase Y, & Aonuma H (2019) Different synchrony in rhythmic movement caused by morphological difference between five-and six-armed brittle stars. *Sci Rep* **9**, 8298. https://doi.org/10.1038/s41598-019-44808-w.

Wakita D, Kagaya K, & Aonuma H (2020) A general model of locomotion of brittle stars with a variable number of arms. *J Royal Soc Interface* **17**, 20190374. https://doi.org/10.1098/rsif.2019.0374.

International conferences

Wakita D & Aonuma H (November, 2017) Morphological regeneration and functional recovery in the fissiparous brittle star *Ophiactis* sp. 18th RIES-Hokudai International Symposium (Sapporo, Japan) [poster].

Wakita D, Hayase Y, & Aonuma H (May, 2018) Rhythmic movement of the disk in the green brittle star *Ophiarachna incrassata*. 16th International Echinoderm Conference (Nagoya, Japan) [oral].

Wakita D, Hayase Y, & Aonuma H (November, 2018) Approach to non-neural interaction coordinating rhythmic movement in brittle stars. 6th International Life-Science Symposium (Sapporo, Japan) [oral].

Wakita D & Aonuma H (December, 2018) Number and function of radially symmetric arms in the locomotion of brittle stars. 19th RIES-Hokudai International Symposium (Sapporo, Japan) [poster].

Wakita D & Aonuma H (August, 2019) Attempt to identify body structure generating a balloon-like rhythmic movement in the green brittle star. 1st Symposium on Invertebrate Neuroscience (Tihany, Hungary) [oral].

Wakita D, Kagaya K, & Aonuma H (September, 2019) Common walking rule among four-, five-, six-, and seven-armed brittle stars. 10th European Conference on Echinoderms (Moscow, Russia) [oral].

Wakita D, Kagaya K, & Aonuma H (December, 2019) How does a radially symmetrical animal decide movement direction? 20th RIES-Hokudai International Symposium (Sapporo, Japan) [poster].

Domestic conferences

脇田大輝，早瀬友美乃，青沼仁志（2017 年 12 月）Radial symmetry plays a rhythm in the green brittle star. 第 14 回棘皮動物研究集会（山口県山口市）［口頭］.

脇田大輝，青沼仁志（2018 年 12 月）5 腕と 6 腕のクモヒトデ：歩き方の法則は？　第 15 回棘皮動物研究集会（神奈川県横浜市）［口頭］.

脇田大輝，浪花啓右，早瀬友美乃，青沼仁志（2019 年 1 月）オオクモヒトデの盤の自律分散協調システム．第 31 回自律分散システム・シンポジウム（大阪府吹田市）［口頭］.

Lecture

Wakita D (August, 2018) How shape makes motion? Learning from individual difference in brittle stars. Sakura Science, Japan Science and Technology Agency. Hokkaido University (Sapporo, Japan).

Grants

Wakita D (September, 2018 – February, 2019) Animal out of Neurons—Robot out of Electricity. Nitobe School Project Grant. Hokkaido University Frontier Foundation.

脇田大輝（2019 年 4 月～2020 年 2 月）クモヒトデの五放射相称の身体を協調させる神経ネットワークに関する研究．笹川科学研究助成．日本科学協会.

Award

Wakita D (December, 2017) Poster Award. 18th RIES-HOKUDAI International Symposium.